

A Bezier Based Higher Order Panel Method for
Steady Flow Analysis of Lifting and Non-Lifting Bodies

by

Edmund B. Roessler

B.S., Naval Architecture and Marine Engineering
Webb Institute, 1985

Submitted to the Department of Ocean Engineering
in Partial Fulfillment of the Requirements for the Degree of
Master of Science in Naval Architecture and Marine Engineering

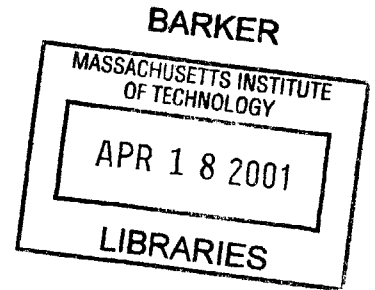
at the

Massachusetts Institute of Technology

February 2001

© 2001 Edmund B. Roessler. All rights reserved.

The author hereby grants MIT permission to reproduce and to distribute publicly paper and electronic copies of this thesis document in whole or in part.



Signature of Author: _____
Department of Ocean Engineering
February 8, 2001

Certified by: _____
Justin E. Kerwin
Professor of Naval Architecture
Thesis Supervisor

Accepted by: _____
Professor Nicholas Patrikalakis
Kawasaki Professor of Engineering
Chairman, Department Committee on Graduate Studies

A Bezier Based Higher Order Panel Method for Steady Flow Analysis of Lifting and Non-Lifting Bodies

by

Edmund B. Roessler

Submitted to the Department of Ocean Engineering
on February 8, 2001, in partial fulfillment of the
requirements for the Degree of Master of Science in
Naval Architecture and Marine Engineering

ABSTRACT

A three-dimensional variable-order panel method utilizing Bezier surfaces and functions for representation of body geometry and distribution of velocity potential in steady incompressible flow applications is presented. A prototype implementation of the method is demonstrated for steady flow past spheroids, including computation of added mass components for a range of beam-length ratios. Very good agreement with exact values is demonstrated. Considerations for extending the method to the lifting-body case are discussed in detail.

The thesis describes the use of both triangular and tensor-product (four-sided) Bezier patches in the panel method, and discusses the advantages that may be obtained in relation to modeling of a hydrofoil tip region. Included is a sample discretization of a hydrofoil.

A panel-coupling technique (*velocity coupling*) is utilized in order to improve overall solution accuracy. Whereas continuity of potential is automatically guaranteed at panel interfaces, velocity coupling ensures continuity of velocity at prescribed nodes. The velocity-coupling technique introduces an alternate form of independent equation, used in lieu of the boundary integral equation at appropriate locations, and is found to be much faster to assemble in comparison to the integral equation.

Thesis Supervisor: Justin E. Kerwin
Title: Professor of Naval Architecture

Acknowledgments

Prof. Jake Kerwin deserves special thanks for suggesting a thesis topic based on a higher-order panel method in the first place, and then pointing me in the right direction when things might otherwise have veered off course. My understanding of Green's theorem owes much to Prof. Paul Sclavounos, whose insight helped shape the content of this thesis.

Thanks must go to the professors, research engineers and students who helped me learn about hydro- and aerodynamics, propellers, computational fluid dynamics, boundary-layer theory, turbomachinery, heat exchangers, adaptive structures, surface waves and other good stuff.

My gratitude extends to Peter Gwyn for fostering a pro-education philosophy at Rolls Royce Naval Marine.

Without my parents, who have always been there and continue to take a keen interest, I wouldn't have anyone to thank.

My wife Colette receives the biggest thanks for putting up with my computational antics.

Contents

1	Introduction	11
2	Overview of Potential-Based Boundary Integral Formulation	15
2.1	Boundary-value Problem for Incompressible Potential Flow	16
2.1.1	Potential Flow Governing Equations	16
2.1.2	Kutta Condition	19
2.1.3	Boundary Conditions	20
2.1.3.1	Body Boundary	20
2.1.3.2	Wake Boundary	21
2.1.3.3	Far Boundary	22
2.2	Boundary Integral Equation	23
2.2.1	Basic Integral Equation	25
2.2.2	Boundary Integral Equation	27
2.2.2.1	Total Potential Formulation	27
2.2.2.2	Perturbation Potential Formulation	28
3	Fundamentals of Bezier Curves, Surfaces and Functions	29
3.1	Historical Background	29
3.2	Bernstein Polynomials	30
3.3	Bezier Curves and Functions	31
3.3	Bezier Surfaces and Related Functions	33
3.3.1	Tensor-product Bezier Surfaces and Functions	34
3.3.2	Triangular Bezier Surfaces and Functions	35
4	Bezier Based Higher Order Panel Method	39
4.1	Body and Wake Surface Discretization	39
4.2	Bezier Modeling of Surface Geometry	41
4.3	Bezier Modeling of Potential Distribution	41
4.4	The Discrete Form of the Boundary Integral Equation	43
4.4.1	Total Potential Formulation	44
4.4.2	Perturbation Potential Formulation	49
4.5	Avoiding Singularity Problems in the Induction Integrals	50
4.6	Quadrature Tests	52

4.7	Velocity Coupling	63
4.7.1	Velocity Coupling Equation	65
4.8	Assembly of Linear System of Equations	65
4.8.1	Boundary Integral Equation	66
4.8.2	Velocity-coupling Equation	66
4.8.3	Kutta Condition	67
4.9	Solution of Matrix Equation	69
4.10	Velocity Computation	69
5	Test Cases	71
5.1	Steady Flow Past Sphere	71
5.2	Added Mass of Spheroids	73
5.3	Sample Discretization of Hydrofoil	77
6	Conclusions	79
	Bibliography	81

List of Figures

- 2.1 Schematic section of three-dimensional potential flow domain and boundary.
- 3.1 Bernstein polynomials of degree 3.
- 3.2 A Bezier curve of degree 4 and its associated Bezier polygon.
- 3.3 A Bezier function.
- 3.4 Barycentric or area-based coordinates.
- 3.5 Bezier control points associated with base triangle (case of $n = 3$).
- 4.1 Domain of unit planar QUAD panel used in single-panel quadrature test.
- 4.2 Domain of unit planar TRI panel used in single-panel quadrature test.
- 4.3 Domain of spherical QUAD panel used in single-panel quadrature test.
- 4.4 Domain of spherical TRI panel used in single-panel quadrature test.
- 4.5 Errors using standard Gauss-Legendre quadrature in computation of the potential induced by a constant-strength source distribution over a *planar* square-shaped QUAD patch, with singularity (field point) located at a corner node (see Fig. 4.1). Error is independent of patch size and degree of Bezier surface. No error occurs in the computation of the potential induced by a constant-strength normal dipole; the computed value agrees with the exact value (identically zero in this case).
- 4.6 Error using standard Gauss-Legendre quadrature in computation of the potential induced by a constant-strength source distribution over a *planar* square-shaped QUAD patch, with singularity (field point) located at a corner node (see Fig. 4.1). Patch is subdivided into separate equally-sized quadrature domains, as indicated. Error is independent of patch size and degree of Bezier surface.

No error occurs in the computation of the potential induced by a constant-strength normal dipole; the computed value agrees with the exact value (identically zero in this case)
- 4.7 Error using standard Gauss-Legendre quadrature in computation of the potential induced by a constant-strength source distribution over a *planar* TRI patch, with singularity (field point) located at a vertex node (see Fig. 4.2). Patch is subdivided into separate equally-sized quadrature domains, as indicated. Error is independent of patch size and degree of Bezier surface.

No error occurs in the computation of the potential induced by a constant-strength normal dipole; the computed value agrees with the exact value (identically zero in this case)

- 4.8 Errors using standard Gauss-Legendre quadrature in computation of potential induced by constant-strength source distribution over a *spherical* QUAD patch, with field point (singularity) located at a corner node (see Fig. 4.3). Patch is Bezier surface of degree 4, varying in size (in terms of solid angle) as shown. Patch is not subdivided into multiple quadrature subdomains. Results are similar for the potential induced by a constant-strength normal dipole.

Results from [Aliabadi 89] using *weighted* Gaussian integration are shown for comparison.

- 4.9a Schematic of trailing edge discretization. The trailing edge is a closed curve as denoted by C_{TE} .
- 4.9b Close-up of panel nodes at the trailing edge, near the end of the wing span. Opposing trailing edge nodes are joined by dotted lines. For a zero-thickness trailing edge ($t_{TE} = 0$), opposing nodes occupy the same location; in this figure they are shown separated to clarify the different treatment of the nodes.
- 5.1 Discretization of spherical body, 8 x 8 panels (meridional x circumferential).
- 5.2 Comparison of computed and exact potential (total) and meridional velocity for spherical body shown in Fig. 5.1.
- 5.3 Discretization of spheroid. Beam-length ratio = 0.3. Panel Discretization: 8 x 8.
- 5.4 Added-mass coefficient m_{11} for a spheroid of length $2a$ and midbody diameter of $2b$. Bezier degree 3 for both surface and potential function. The added mass m_{11} denotes surge acceleration (longitudinal direction). The coefficient is nondimensionalized with respect to the mass of the displaced volume of fluid, which is $(4/3)\pi\rho ab^2$. See [Newman 77] for further details.
- 5.5 Added-mass coefficient m_{22} for a spheroid of length $2a$ and midbody diameter of $2b$. Bezier degree 3 for both surface and potential function. The added mass m_{22} denotes sway acceleration (lateral, in equatorial plane). The coefficient is nondimensionalized with respect to the mass of the displaced volume of fluid, which is $(4/3)\pi\rho ab^2$. See [Newman 77] for further details.
- 5.6 Added-mass coefficient m_{55} for a spheroid of length $2a$ and midbody diameter of $2b$. Bezier degree 3 for both surface and potential function. m_{55} denotes the added moment of inertia for rotation about an axis in the equatorial plane. The coefficients are nondimensionalized with respect to the moment of inertia of the displaced volume of fluid, which is $(4/15)\pi\rho ab^2(a^2 + b^2)$. See [Newman 77] for further details.
- 5.7 Sample discretization of a symmetrical-section hydrofoil with elliptical planform, showing use of TRI panels at both ends of the span.

List of Tables

- 4.1 Summary of single-panel quadrature tests.
- 4.2a Quadrature test errors (percent) obtained for *spherical* TRI panel, with $\theta = 0.1$ degree and various α .
- 4.2b Quadrature test errors (percent) obtained for *spherical* TRI panel, with $\alpha = 0.1$ degree and various θ .
- 4.2c Quadrature test errors (percent) obtained for *spherical* TRI panel, for $\theta = \alpha$.

Chapter 1

Introduction

Panel methods have been utilized extensively in aerodynamic and hydrodynamic design for several decades, beginning with the classic three-dimensional panel method developed by Hess and Smith in the 1960's [Hess 67]. This method was initially based on constant-strength sources and vortices on flat quadrilateral panels ('surface elements') distributed over the body; the adoption of these surface elements facilitated discretization of an arbitrary body surface and made it possible to analyze flows past realistically-shaped bodies. Since that time, a large number of variations on the original approach have been devised, although most can be classified as either velocity-field or potential-field formulations [Lee 87]. The first potential-field formulation as adapted to the lifting-body problem is attributed to Morino, whose implementation utilized a constant value of potential over each panel [Morino 74]. With the goal of increasing solution accuracy and computational performance, a number of so-called higher-order panel methods began to appear in the 1980's, e.g. [Hess 87]. However, many well-known codes still employ constant-strength panels (the latter sometimes being referred to as a low-order method); this reflects an on-going debate as to whether higher-order methods pose any real advantages over the low-order methods.

Generally speaking, a low-order method requires a substantially greater number of panels than that of a higher-order method, however, as the latter requires a greater number of degrees of freedom (unknowns) per panel, the overall size of the linear system of equations is not necessarily smaller for the higher-order method. This is one reason why comparing low-order and high-order panel methods is difficult at best.

Over the past decade researchers have addressed serious concerns as to the accuracy and convergence of low-order panel methods when applied to certain types of propeller blade

geometry, e.g., see [Hsin 91], [Pyo 94] and [Lee 99]. Such interest is indicative of further work to be done in this area.

In this thesis, a higher-order potential-based panel method utilizing Bezier basis functions is presented. The paper describes a method which incorporates variable-degree Bezier modeling, not only for representation of the surface geometry, but also for the distribution of the velocity potential. The Bezier-based approach was inspired by a B-Spline higher-order method proposed by Lee and Kerwin [Lee 99] and still under development.

In modern computer-aided geometric design (CAGD), B-spline basis functions do in fact present a more powerful means of surface representation compared to Bezier surfaces, especially for complex configurations like ship hulls. Today, B-spline-based NURBS¹ surfaces are utilized as the de facto industry standard. On the other hand, a panel method, by definition, considers a discretization of the boundary into a collection of panels, and the complexity of each individual panel is far less than that of the surface as a whole. Individual panels can therefore be adequately represented using Bezier patches. Moreover, with respect to surface discretization, the Bezier formulation offers a distinct advantage over B-spline surfaces, in that Bezier patches can be rendered in both triangular and tensor-product (four-sided) forms.² The availability of both types of patches gives the analyst more flexibility in choosing panel configurations, as for example, in the modeling of a hydrofoil or propeller tip. A sample discretization of a hydrofoil is included herein to illustrate one possibility.

Some well-known panel codes in use today utilize panels that do not have conforming interfaces (e.g., neighboring panels connect at only one point along the edge). Using Bezier patches, it is a simple and straightforward matter to maintain full continuity of the surface along the entire perimeter of each panel, whether triangular, tensor-product or a combination of both types is used.

1. NURBS: Non-uniform rational B-splines

2. The author is not aware of any B-spline techniques for triangular surface representation.

The present paper begins with a brief review of the fundamentals of potential-based panel methods. This is followed by a review of the fundamentals of Bezier curves, surfaces and functions in Chapter 3. Both triangular and tensor-product Bezier surfaces are addressed, as well as their role in representing scalar functions (potential distribution). The method for computing velocity via first-derivative computations of the Bezier surface and function is also presented.

The objective of this thesis is to develop a general-purpose variable-order method for application to non-lifting and lifting bodies in steady incompressible inviscid flow, including the important problem of predicting added mass.³ The method has been tested using a first-generation implementation coded in C++ using object-based technology. Computed results are compared with exact values for two applications: *a*) steady flow past a sphere and *b*) added mass of spheroid (ellipsoids of revolution). Very good agreement is demonstrated in both cases, as seen in Chapter 5.

A preliminary formulation for the lifting-body case is presented, however, further development and testing is required in order to ascertain the validity of the method for this problem domain. Various modeling issues and other considerations in the lifting-body problem are discussed in some detail.

A panel-coupling technique referred to as *velocity coupling* is utilized to improve overall solution accuracy, and to eliminate or minimize the need for ‘velocity-smoothing’ or finite differencing operations on the potential during post processing. Whereas continuity of potential is automatically guaranteed at panel interfaces, velocity coupling ensures continuity of velocity at prescribed nodes. The velocity-coupling technique introduces an alternate form of independent equation, applied in lieu of the boundary integral equation at appropriate locations, and is found to be much faster to assemble in comparison to the integral equation.

3. The concept of added mass is usually associated with unsteady applications, however it is also a valuable concept in certain steady-flow applications, e.g., the correction of the measured drag coefficient in wind tunnels with diverging walls. In any case, the computation of the added mass itself is a *steady* problem.

Although the resulting matrix equation is hybrid in form, to date no solvability problems have been encountered through the use of this technique, when applied in the manner described in Chapter 4.

Results of this initial investigation indicate that further development work on the Bezier-based panel method may be warranted, depending on the target application. Its applicability as an analysis tool for use ultimately in propeller blade design and analysis, for example, remains an open question, however there appear to be no technical limitations to preclude it from being developed toward that purpose. The Bezier-based method may be of utility in other fields in which boundary element techniques are commonly utilized.

Chapter 2

Overview of Potential-Based Boundary Integral Formulation

The boundary element or *panel* method is founded on Green's theorem, the well-known group of theorems that express equivalence between an integral over a domain in n dimensions to an integral over a domain in $(n-1)$ dimensions.⁴ The boundary integral equation resulting from Green's theorem makes it possible to obtain solutions to three-dimensional boundary value problems via surface (boundary) discretization alone. For a large class of engineering problems, the boundary integral equation relieves one from the arduous task of performing a discretization of a volumetric domain, e.g., as in the finite element method. The comparative simplicity afforded by the boundary integral equation has long been a prime motivating factor driving the development of panel methods.

The starting point for the Bezier-based higher-order panel method described in Chapter 4 is a *potential-based* boundary integral equation, rather than a source-distribution integral equation. The latter was the basis of the original three-dimensional panel method developed by Hess and Smith in the early 1960's [Hess 64]; subsequently, a panel method using a potential-field formulation was developed by Morino [Morino 74]. In principle, both methods yield identical solutions for the potential function, as discussed in [Sclavounos 87]. The potential-based method was selected for this thesis based on considerations discussed in [Kerwin 87].⁵ Accordingly, this chapter will focus on the potential-based boundary integral formulation.

Before reviewing the boundary integral equation, the boundary-value problem for incompressible potential flow is discussed.

-
4. In general, Green theorems are equivalent to integration by parts. [Arfken 85] refers to Green's theorem as a "corollary of Gauss's theorem."
 5. Other variations of these two formulations are discussed in this reference as well.

2.1 Boundary-value Problem for Incompressible Potential Flow

The primary task of the panel method described herein is the numerical computation of the unknown distribution of potential on the body boundary. Once the distribution of potential is computed, the potential-flow velocity and pressure fields may be determined. Before computation of the potential can proceed, a boundary-value problem (BVP) must be defined in suitable terms so that a corresponding matrix equation can be constructed and solved. Generally, the closer the match between the matrix equation and the BVP, the more reliable the solution, provided the BVP is well-posed to begin with.

The process of defining a BVP requires identification of the governing equations and boundary conditions characterizing the problem. The theory underlying potential-flow boundary-value problems is well known, e.g., see [Kellogg 29], [Lamb 32], [Hess 67], [Hess 72], [Morino 74], [Newman 77], [Hunt 80], [Moran 84], [Lee 87], [Kerwin 87], and [Hsin 90]. Accordingly, only a brief overview is provided here.

2.1.1 Potential Flow Governing Equations

The problem domain under consideration is the steady potential flow about a three-dimensional *lifting* or *non-lifting* body in an unbounded incompressible, inviscid fluid. The body is assumed to be rigid and held fixed with respect to an inertial coordinate system, and subject to an inflow velocity U_∞ , as shown in Figure 2-1.

For analysis purposes a domain $\bar{\Omega} = \Omega \cup \partial\Omega$ is considered, where Ω is an open simply-connected⁶ region with boundary $\partial\Omega$ subdivided as

$$\partial\Omega = S_B \cup S_\infty \cup S_W, \quad (2.1)$$

where

S_B is the body boundary.

S_∞ is a surface located far from the body and “surrounding” the body.

6. A ‘simply-connected’ region is one such that all circuits drawn within it are reducible. A circuit is said to be reducible if it is capable of being contracted to a point without passing out of the region. See [Lamb 32].

S_W is a branch surface connecting S_B and S_∞ . S_W represents an infinitesimally thin trailing-vortex sheet shed from the trailing edge of a lifting body [Kerwin 87]. For non-lifting bodies, S_W can be regarded as a tube of infinitesimal radius, yielding no contribution to the boundary integral equation, e.g. see [Newman 77].

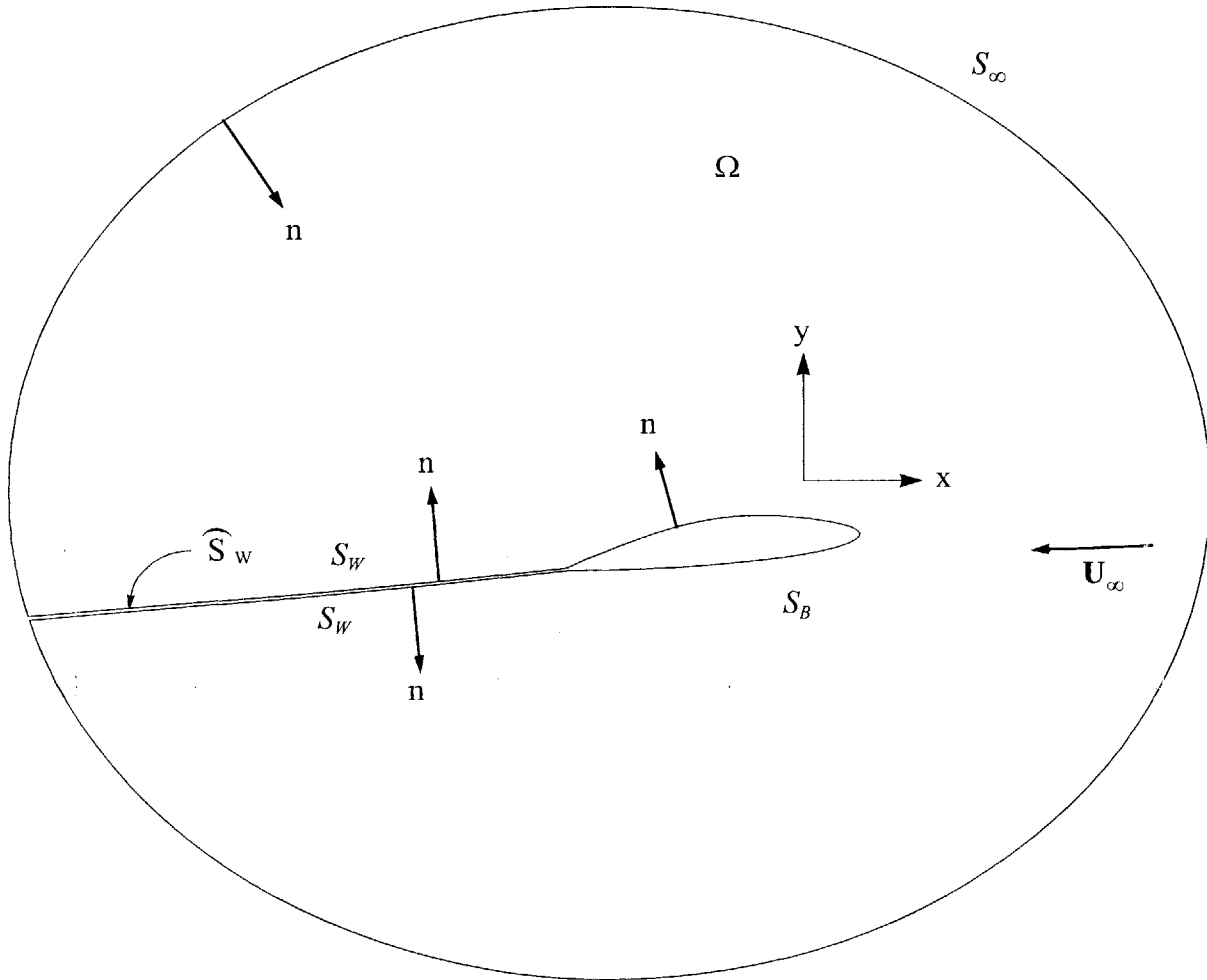


Fig. 2.1 Schematic section of three-dimensional potential flow domain and boundary.

Strictly speaking, $\partial\Omega$ does not actually enclose the body, i.e., the body itself is not contained within the domain.⁷ It should be noted that S_W is, conceptually speaking, a ‘hollow cylinder’; the cross-section of this cylinder is distorted according to the manner in which the flow is

7. For explanatory purposes, and to help fix ideas, the domain boundary may be compared to the *inside* surface of a large inflated balloon. At some location on the outer surface of the balloon a relatively tiny body is displaced toward the center of the balloon and held in place, without penetrating the balloon surface. The region of the balloon in contact with the body becomes S_B , and the remaining portion displaced inward becomes the branch surface S_W .

anticipated to detach from the tail end of the body. In the case of a lifting body (e.g., hydrofoil) with zero thickness at the trailing edge, S_W has the outward appearance of a sheet, however, is actually the hollow cylinder in a ‘flattened state’. This configuration is necessary, not only to satisfy the requirement that the flow region be simply-connected, but also to facilitate a differential of potential between the upper and lower sides of the lifting body. Normal vectors to the boundary are defined as shown in Figure 2.1 (i.e., pointing toward the interior of the domain). In view of the foregoing discussion regarding S_W , it is normal practice to assign a normal vector to one side of S_W only, for the lifting-body problem. See Section 2.1.3.2 below.

Within Ω , the flow is assumed to be irrotational, i.e., the vorticity ω is zero:

$$\omega = \nabla \times \mathbf{V} = 0 \quad \text{in } \Omega. \quad (2.2)$$

This assumption is based on certain premises. For the purpose of this thesis, the flow upstream of the body is assumed to be irrotational; then, according to Kelvin’s theorem, a material volume of fluid upstream of the body and initially irrotational will remain irrotational as the material volume moves over the body [Newman 77]. Lack of a no-slip condition at the body boundary and the assumption of an infinitesimally thin wake downstream of the body are abstract simplifications of the true viscous flow. Real viscous flows are characterized by the presence of boundary layers and viscous wakes; however, the slip-boundary and thin-wake assumptions present a reasonable approach for modeling of real non-separated flows over streamlined bodies.

The irrotationality assumption implies the existence of a unique scalar potential field, such that the velocity field \mathbf{V} may be expressed as the gradient of a *total potential* Φ :

$$\mathbf{V} = \nabla \Phi. \quad (2.3)$$

Alternatively, the velocity field may be expressed in terms of a *perturbation potential* ϕ , whereby

$$\mathbf{V} = \mathbf{U}_\infty + \mathbf{v} = \mathbf{U}_\infty + \nabla\phi , \quad (2.4)$$

and \mathbf{v} is the disturbance velocity field corresponding to the perturbation potential. As pointed out in [Hess 67], utilization of the perturbation potential permits somewhat greater generalization in the types of flows to be considered, since the onset velocity field \mathbf{U}_∞ is not necessarily restricted to the class of irrotational flows.

Of the three conservation laws (mass, momentum and energy), only the first is needed in the formulation of the potential-flow boundary-value problem. With the restrictions stated herein, mass continuity is given by Laplace's equation, in terms of the potential (either form):

$$\nabla^2\Phi = 0 \text{ in } \Omega \quad (\text{total potential}) \quad (2.5)$$

$$\nabla^2\phi = 0 \text{ in } \Omega \quad (\text{perturbation potential}) \quad (2.6)$$

2.1.2 Kutta Condition

The lifting-body problem requires an auxiliary condition (Kutta condition) to ensure the existence of a finite velocity at the trailing edge. In its most general form the Kutta condition is given as

$$\nabla\Phi < \infty \quad \text{at the trailing edge of the body} . \quad (2.7)$$

The same principle applies for the perturbation potential. The Kutta condition numerically constrains the potential in such a manner as to ensure a physically plausible flow field at the trailing edge, and the amount of circulation and lift generated by the body is restricted accordingly.⁸

8. The relationship between circulation and lift is governed by the Kutta-Joukowski theorem. See, e.g., [Newman 77]. The circulation is defined as the line integral of the tangential component of the velocity along any closed curve (as may surround a hydrofoil):

$$\text{Lift } L = \rho U_\infty \Gamma, \quad \text{where circulation } \Gamma = \oint \mathbf{V} \cdot d\mathbf{s}$$

2.1.3 Boundary Conditions

Typically, two types of boundary conditions are specified on $\partial\Omega$, viz., Dirichlet and Neumann conditions. The former is synonymous with a known or specified *potential* and the latter refers to a known or specified *normal gradient* of the potential.⁹ The need for these boundary conditions becomes obvious when examining the boundary integral equation, discussed in Section 2.2. On a given region of $\partial\Omega$ one is not ordinarily permitted to prescribe both a Dirichlet and a Neumann condition, however there are exceptions. In the usual case, both forms will be specified on their respective regions of the boundary, and no part of the boundary will lack one or the other.

The following sections address boundary conditions on S_B , S_W and S_∞ , respectively.

2.1.3.1 Body Boundary

Typically, Dirichlet conditions are not specified on the body boundary, simply because the potential is unknown.¹⁰ Therefore, Neumann conditions must be specified on the body boundary. In the context of potential flow applications, a Neumann condition is equivalent to the kinematic boundary condition. Assuming the body is solid (i.e., no transpiration), the kinematic boundary condition follows from the condition that the flow at the body boundary must be tangent to the body surface. For the total potential, the Neumann condition is

$$\frac{\partial\Phi}{\partial n} = \mathbf{n} \cdot \nabla\Phi = \mathbf{n} \cdot \mathbf{V} = 0 \quad \text{on } S_B. \quad (2.8)$$

Using (2.4), the Neumann condition for the perturbation potential is

$$\frac{\partial\phi}{\partial n} = \mathbf{n} \cdot \nabla\phi = -\mathbf{n} \cdot \mathbf{U}_\infty \quad \text{on } S_B. \quad (2.9)$$

9. The terms ‘essential’ and ‘natural’ are interchangeable with Dirichlet and Neumann, respectively.

10. This is the motivation behind the panel method in the first place!

2.1.3.2 Wake Boundary

Boundary conditions on the branch surface S_w depend on whether the body is lifting or non-lifting. In the analysis of a non-lifting body, S_w is usually reduced to a tube of infinitesimal radius, as described in [Newman 77]. In this case, there is no contribution to the integral equation from S_w ; certainly, there is no surface upon which any boundary condition could be prescribed. Although the ‘utilization’ of an infinitesimally small tube results in certain simplifications, it is not strictly required; other configurations of the ‘wake’ of a non-lifting body are conceivable.

Dirichlet conditions come into play in the analysis of a lifting body. The branch surface S_w is interpreted as a variable strength ‘dipole sheet’ equivalent to an idealization of the free trailing vortex system emanating from the trailing edge of the body.¹¹ For convenience, \widehat{S}_w denotes one-half of the wake boundary circumference (corresponding to either the ‘upper’ or ‘lower’ side), while S_w refers to the entire wake boundary circumference (or loosely speaking, both ‘sides’ of the wake sheet). Here, \widehat{S}_w is assigned to the ‘upper’ side of the lifting body, so that its normal vector is facing more or less in the positive y direction (see Fig. 2.1). For the purpose of this thesis, the position of the wake sheet is either known or assumed; regardless, the locations of all surfaces (i.e., the entire boundary $\partial\Omega$) are considered known and fixed, and a solution to the *direct* problem is sought (in contrast to the inverse problem, in which the position of a portion of the boundary is unknown and being sought, inevitably necessitating some kind of iterative procedure).

On the wake sheet, Dirichlet conditions cannot be specified explicitly, as the potential is unknown on S_w . However, the *difference* in potential at any point on S_w is expressible in terms of the potential at the trailing edge, as discussed in [Morino 74]. This ‘implicit’ Dirichlet condition is tied in with the Kutta condition, since the Kutta condition can be expressed in terms of the potentials on either side of the foil at the trailing edge. As the flow over the suction and pressure sides proceeds downstream from the leading edge stagnation

11. There is equivalence between the rate of change of the normal dipole strength along the surface, and the strength of a vortex tangent to the surface (orientated perpendicularly to the dipole array). For further details, see [Hess 72].

point, the value of the potential changes, resulting in a more or less cumulative increase in the potential difference as the trailing edge is approached. This assumes the body is generating lift – the potential difference at the trailing edge is zero for a non-lifting body. As the wake of a foil is not able to sustain a pressure difference, no further change in the potential difference occurs as the flow leaves the trailing edge. *Whatever potential difference has accrued at the trailing edge is all there will be, and the difference is maintained as the flow proceeds away from the body.*

Further aspects of the wake boundary and Kutta condition are discussed in Section 2.2 and Chapter 4.

2.1.3.3 Far Boundary

Treatment of the far boundary S_∞ depends on whether the total or perturbation potential is utilized. This is one region in which both Dirichlet and Neumann conditions apply, and since both the potential and the normal gradient are known on S_∞ , the corresponding surface integral in the boundary integral equation can be computed and reduced to a simple quantity. As the perturbation potential is easier to deal with, it is discussed first.

On the far boundary S_∞ , both the perturbation potential and the normal gradient of the potential are expected to vanish in the limit as the distance between the surface and body approaches infinity:

$$\phi \rightarrow 0, \quad \text{at infinity}, \quad (2.10)$$

and

$$\nabla\phi \rightarrow 0, \quad \text{at infinity}. \quad (2.11)$$

Considering this hypothetical boundary for S_∞ , there is no contribution to the integral equation and consequently no further consideration is required with respect to boundary conditions at the far boundary.

For the total potential, matters are somewhat more complicated, but reconcilable. Neither the total potential nor the normal gradient (i.e., the velocity) vanish everywhere on S_∞ . However, these quantities are known, provided the geometry of S_∞ is specified and the distance between the body and S_∞ is sufficiently large so that any disturbance due to the presence of the body may be regarded as negligible, i.e.,

$$\Phi \rightarrow \Phi_\infty, \quad \text{at infinity,} \quad (2.12)$$

and

$$\nabla\Phi \rightarrow \mathbf{U}_\infty, \quad \text{at infinity.} \quad (2.13)$$

It turns out that the corresponding surface integral in the integral equation evaluates to a simple quantity proportional to the incident potential Φ_∞ .¹² Using the resulting simplified form of the boundary integral equation for the total potential, again, no further consideration is required with respect to boundary conditions at the far boundary.

2.2 Boundary Integral Equation

The boundary integral equation is the backbone of the panel method. As pointed out by [Robertson 65], the significance of integral equations is the *equivalence theorem*, which states:

The solution of an integral equation is a solution of the corresponding boundary-value problem and vice versa.¹³

By casting the governing equation (2.5) or (2.6) into an boundary integral equation, a solution can be obtained by considering what is happening on the boundary $\partial\Omega$ alone, while disregarding details within the domain Ω itself. The overall simplification and resulting economy

12. It can be shown that for a sphere surrounding the body, the Dirichlet condition contributes two-thirds toward Φ_∞ , while the Neumann condition contributes the remaining one-third. The Dirichlet and Neumann conditions are associated with the dipole and source terms, respectively, in Green's formula.

13. This, according to [Robertson 65], is demonstrated in Courant and Hilbert (Methods of Mathematical Physics, 1st English ed., Interscience Publishers, 1953) with the aid of Green's function.

of effort achieved with the integral equation is significant in comparison to the original boundary value problem (differential equation).

From the standpoint of implementing a panel code, the main purpose of the boundary integral equation is to provide a means for generating a system of linear algebraic equations to be solved in order to yield the distribution of potential on the body boundary.

In this section, only the *potential-based* boundary integral equation is addressed. For discussion purposes, it is useful to distinguish between the *basic* integral equation and the *boundary* integral equation. The basic integral equation is a Fredholm equation of the second kind¹⁴ giving the potential at a point anywhere within the domain Ω , in terms of the potential and its normal derivatives on the boundary. The basic integral equation suffers from the fact that it becomes *strongly singular*¹⁵ if the field point (i.e., the point at which the unknown potential is sought) lies on the boundary. Nonetheless, the basic integral equation is important in two respects:

1. The boundary integral equation is derived from the basic integral equation;
2. The basic integral equation can be used to compute the potential away from the boundary after the boundary solution is obtained.

The ‘boundary integral equation’ refers to an integral equation of the second kind in which the potential is expressed entirely in terms of values on the boundary $\partial\Omega$. The boundary integral equation is essentially ‘de-singularized’, as the kernel does not, strictly speaking, become infinite at any point in the range of integration. De-singularization is accomplished by integrating over an infinitesimal region S_ϵ surrounding the field point, yielding a free value of potential which is simply added to the original term located outside the integral. This process subsequently alters the range of integration, since the integral has already been evaluated over S_ϵ . Therefore S_ϵ must be excluded, in a manner analogous to the Cauchy principal integral.¹⁶

14. A Fredholm integral equation is a linear integral equation in which the limits of integration are fixed. An integral equation of the second kind is one in which the unknown function appears both inside and outside the integral(s). For more details, see, e.g., [Arfken 85].

15. There are two types of kernels encountered in this application. Both types are strongly singular as they contain a difference term $(x - \xi)^\alpha$ in the denominator, with $\alpha = 1$ and $\alpha = 2$, respectively. The former is referred to a Cauchy singularity. See, e.g., [Jerri 99].

The basic integral equation can be deduced in several ways. The traditional approach employs the symmetrical form of Green's theorem. A modern approach uses the concept of distribution, which according to [Brebbia 89], "illustrates the degree of continuity required of the functions and the importance of the accurate treatment of the boundary conditions."

No derivations of the basic integral equation or boundary integral equation are provided herein – various derivations are given in [Newman 77], [Kerwin 87], [Brebbia 89], and [Chari 00]. The basic integral equation is presented in the next section, followed by the boundary integral equations in terms of the total potential and perturbation potential, respectively.

2.2.1 Basic Integral Equation

The basic integral equation, better known as Green's formula or Green's third identity, is given as

$$\Phi(\mathbf{x}) = \iint_{\partial\Omega} \left[G(\mathbf{x}; \xi) \frac{\partial\Phi(\xi)}{\partial n_\xi} - \Phi(\xi) \frac{\partial G(\mathbf{x}; \xi)}{\partial n_\xi} \right] d\xi . \quad (2.14)$$

This equation gives the potential at a field point \mathbf{x} in terms of the potential and normal gradient distribution on the boundary $\partial\Omega$, where integration is performed with respect to the dummy variable ξ . The quantity $G(\mathbf{x}; \xi)$ is defined as

$$G(\mathbf{x}; \xi) = -\frac{1}{4\pi|\mathbf{x} - \xi|} , \quad (2.15)$$

where $|\mathbf{x} - \xi|$ is the distance between position vectors $\mathbf{x} = (x, y, z)$ and $\xi = (\xi, \eta, \zeta)$. Although best known as Green's function, $G(\mathbf{x}; \xi)$ is sometimes called the *fundamental solu-*

-
16. Cauchy's principal value of an integral of a function $f(x)$ that becomes infinite at an interior point $x = x_0$ of the interval of integration (a, b) is the limit

$$\lim_{\varepsilon \rightarrow 0} \left(\int_a^{x_0 - \varepsilon} f(x) dx + \int_{x_0 + \varepsilon}^b f(x) dx \right),$$

where $0 < \varepsilon \leq \min(x_0 - a, b - x_0)$. See [Tricomi 57].

tion, e.g., as in [Brebbia 89], since it is the simplest possible non-trivial solution to the potential-flow governing equation, i.e., (2.5) or (2.6). More specifically, it represents the potential at the field point induced by a unit source at ξ , and for this reason $G(\mathbf{x}; \xi)$ is also referred to as the Rankine singularity. As such, (2.11) satisfies Laplace's equation everywhere except at the source point ξ , so that the fundamental solution can be expressed as

$$\nabla^2 G(\mathbf{x}; \xi) = \delta(\mathbf{x}; \xi), \quad (2.16)$$

where $\delta(\mathbf{x}; \xi)$ is the delta function, i.e.,

$$\delta(\mathbf{x}; \xi) = \begin{cases} 0 & \text{for } \mathbf{x} \neq \xi \\ \infty & \text{for } \mathbf{x} = \xi \end{cases}. \quad (2.17)$$

The delta function has the peculiar but powerful property

$$\int_{-\infty}^{\infty} \delta dx = 1, \quad (2.18)$$

which extends to distributions of functions, so that for a distribution of potential

$$\int_{\Omega} \Phi \delta(\mathbf{x}; \xi) d\xi = \Phi(\mathbf{x}). \quad (2.19)$$

Referring to the second integral in (2.14), the normal gradient of Green's function represents another type of singularity, viz, a *dipole*, which is derivable from the fundamental singularity (source). Whereas a source exhibits no directivity, a dipole has an orientation corresponding to a line on which a source and sink (negative source) approach one another in the limit as the gap approaches zero and the strength of each singularity approaches infinity. By convention, the positive direction is in the direction of the positive source. The normal gradient of Green's function may be expressed more specifically as

$$\frac{\partial G(\mathbf{x}; \boldsymbol{\xi})}{\partial n_{\xi}} = -\frac{(\mathbf{x} - \boldsymbol{\xi}) \cdot \mathbf{n}(\boldsymbol{\xi})}{4\pi|\mathbf{x} - \boldsymbol{\xi}|^3} \quad \text{unit-strength dipole directed along } \mathbf{n}.^{17} \quad (2.20)$$

2.2.2 Boundary Integral Equation

The boundary integral equation is obtained from the basic integral equation by locating the field point on the boundary and evaluating the surface integral in way of the field point by considering an infinitesimally small region S_{ϵ} surrounding the field point. This process is effectively a ‘de-singularization’ of the basic integral equation. The boundary integral equation based on (2.14) is

$$T \Phi(\mathbf{x}) = \int_{\partial\Omega - \partial\Omega_{\epsilon}} \int \left[G(\mathbf{x}; \boldsymbol{\xi}) \frac{\partial\Phi(\boldsymbol{\xi})}{\partial n_{\xi}} - \Phi(\boldsymbol{\xi}) \frac{\partial G(\mathbf{x}; \boldsymbol{\xi})}{\partial n_{\xi}} \right] d\boldsymbol{\xi}. \quad (2.21)$$

The coefficient T is the solid angle (in steradians) subtended at the field point on the boundary, divided by 4π . See, e.g., [Hunt 80]. The usual value for T is $1/2$, corresponding to a smooth continuous surface where the field point is situated. T may vary between 0 and 1, depending on the geometrical configuration of the body boundary and wake surface.

2.2.2.1 Total Potential Formulation

By taking boundary conditions into account as discussed in Section 2.1.3, the resulting boundary integral equation for the lifting-body problem is given as

$$T\Phi(\mathbf{x}) = \Phi_{\infty}(\mathbf{x}) - \int_{S_B - S_{\epsilon}} \int \Phi(\boldsymbol{\xi}) \frac{\partial G(\mathbf{x}; \boldsymbol{\xi})}{\partial n_{\xi}} d\boldsymbol{\xi} - \int_{\widehat{S}_w} \int \Delta\Phi(\boldsymbol{\xi}_{TE}) \frac{\partial G(\mathbf{x}; \boldsymbol{\xi})}{\partial n_{\xi}} d\boldsymbol{\xi}, \quad (2.22)$$

where $\Delta\Phi(\boldsymbol{\xi}_{TE})$ is the difference in potential ‘across’ the trailing edge (i.e., from one side of the wake sheet to the other), with the dummy variable $\boldsymbol{\xi}$ being associated with a position on

17. See, e.g., [Lighthill 86].

the trailing edge, ξ_{TE} , corresponding to the location at which the flow departed the trailing edge.

For the non-lifting problem, the second integral in (2.22) is omitted.

2.2.2.2 Perturbation Potential Formulation

Taking boundary conditions into account as discussed in Section 2.1.3 for the perturbation potential, the resulting boundary integral equation for the lifting-body problem is given as

$$T\phi(\mathbf{x}) = \iint_{S_B - S_e} G(\mathbf{x}; \xi) \frac{\partial \phi(\xi)}{\partial n_\xi} - \iint_{S_B - S_e} \phi(\xi) \frac{\partial G(\mathbf{x}; \xi)}{\partial n_\xi} d\xi - \iint_{\widehat{S}_w} \Delta\phi(\xi_{TE}) \frac{\partial G(\mathbf{x}; \xi)}{\partial n_\xi} d\xi, \quad (2.23)$$

where the meaning of $\Delta\phi(\xi_{TE})$ is described in Section 2.2.2.1 above.

For the non-lifting problem, the last integral in (2.23) is omitted.

Chapter 3

Fundamentals of Bezier Curves, Surfaces and Functions

This chapter presents an overview of Bezier curves, surfaces and functions, elements which form the backbone of the Bezier-based panel method developed in Chapter 4. Most of the information presented here on Bezier curves is based on material explained in [Hoschek 93] and [Farin 99].

3.1 Historical Background

The development of Bezier curves is attributed to P. de Casteljau and P. Bezier, whose efforts were carried out independently on behalf of Citroen (beginning in 1959) and Renault (beginning in 1962), respectively.¹⁸ The introduction of Bezier curves presented an alternative approach to cubic spline techniques developed by J. Ferguson at Boeing in the 1950's.

Only later was it discovered that the curves named after Bezier were intimately connected with the classical Bernstein polynomials; in 1970, R. Forrest discovered that the Bernstein polynomials were indeed the basis functions for Bezier curves. Meanwhile, efforts by de Boor at General Motors led to a practical utilization of B-splines (*basis splines*); although B-splines were actually investigated by I. Schoenberg during World War II, many years passed before an accurate and stable means of computing with B-splines became available. A short time after de Boor's landmark paper, "On calculating with B-splines," appeared in 1972, Gordon and Riesenfeld demonstrated that Bezier curves were a special case of B-spline curves, paving the way for a more unified treatment of the various methods developed on both sides of the Atlantic.

18. According to [Farin 99], 1959 marks the birth of computer-aided geometric design (CAGD), when Citroen hired P. de Casteljau to develop mathematical tools to more fully exploit the capabilities of their numerically-controlled milling machines. De Casteljau invented what he called *Courbes a Poles*, what are now known, ironically, as Bezier curves. P. Bezier learned about Citroen's 'very secretive' efforts and was able to develop a functional CAGD system himself at Renault; his firm allowed him to widely publicize the method.

In this thesis, only the Bezier formulation is considered. The next section begins with a brief description of the Bernstein polynomials. Subsequent sections treat Bezier curves, functions and surfaces.

3.2 Bernstein Polynomials

Bernstein polynomials are the key component in the Bezier representation of curves, surfaces and functions. Bernstein polynomials of degree n are defined as follows:

$$B_r^n \equiv \binom{n}{r} (1-t)^{n-r} t^r, \quad r = 0(1)n. \quad (3.1)$$

The parameter t takes on values anywhere in the closed interval between 0 and 1, i.e., $t \in [0, 1]$. An n^{th} -degree Bernstein polynomial comprises a family of $(n + 1)$ polynomial curves spanning the closed interval $[0, 1]$. All the polynomials are non-negative on this interval. At the end points the values of all the polynomials are zero, except for the first and last polynomials, B_0^n and B_n^n , respectively; the former is equal to 1 at the beginning of the parameter interval ($t = 0$) and the latter is equal to 1 at the end of the interval ($t = 1$).¹⁹

The cubic Bernstein polynomials B_r^3 , for example, take the shape seen in Figure 3.1, for $t \in [0, 1]$.

The Bernstein polynomials form a so-called *partition of unity*, an important property such that the sum of all polynomials is equal to unity for any given value of t in the parameter interval $[0, 1]$, i.e.,

$$\sum_{r=0}^n B_r^n(t) = 1. \quad (3.2)$$

19. Interestingly, a Bernstein polynomial curve is identical to a binomial probability distribution of a random variable, where t is the probability of getting r successes in n trials. Compare (3.1) with the probability distribution formula given, e.g., in [Freund 80].

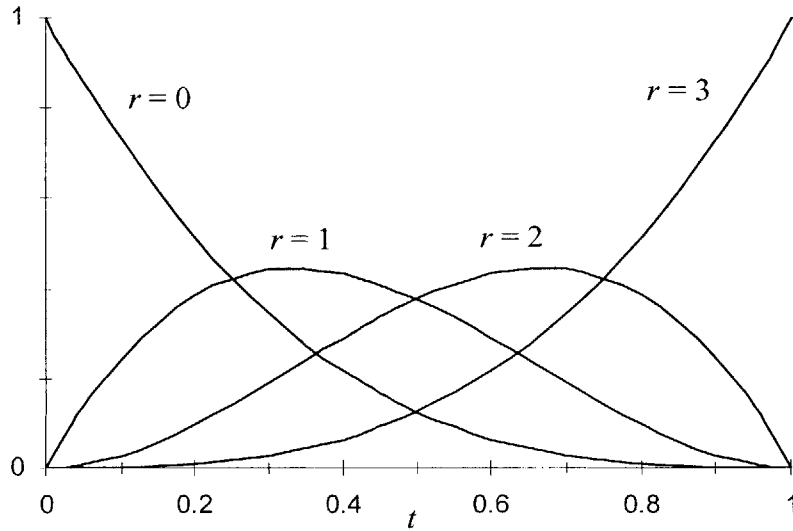


Fig. 3.1 Bernstein polynomials of degree 3.

3.3 Bezier Curves and Functions

A *Bezier curve* can be defined using the Bernstein polynomials as basis functions. A Bezier curve of degree n in parametric form is defined as

$$X(t) = \sum_{i=0}^n \mathbf{b}_i B_i^n(t), \quad (3.3)$$

with coefficients $\mathbf{b}_i \in \mathfrak{R}^d$, $d = 1, 2, 3$. When \mathbf{b}_i are chosen as vectors in \mathfrak{R}^2 or \mathfrak{R}^3 , they are referred to as *Bezier control points* or simply *Bezier points*. If the coefficients \mathbf{b}_i are scalar values, they are called *Bezier ordinates*. The set of straight lines connecting the Bezier points is called the *Bezier polygon*, as shown in Figure 3.2.

The Bezier curve (3.3) is independent of the coordinate system, due to the partition-of-unity property (3.2). If this property did not hold, then a simple translation, rotation or scaling would destroy the relationship between X (the curve) and \mathbf{b} (the Bezier control points).

If the Bezier ordinates b_i are located at parameter values $t = i/n$, then the parametric formula (3.3) for a Bezier curve reduces to a *Bezier function*. See Figure 3.3.

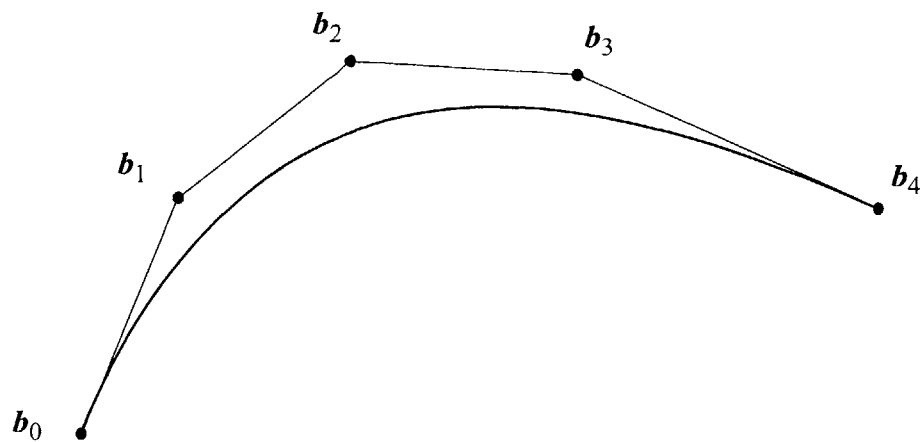


Fig. 3.2 A Bezier curve of degree 4 and its associated Bezier polygon.

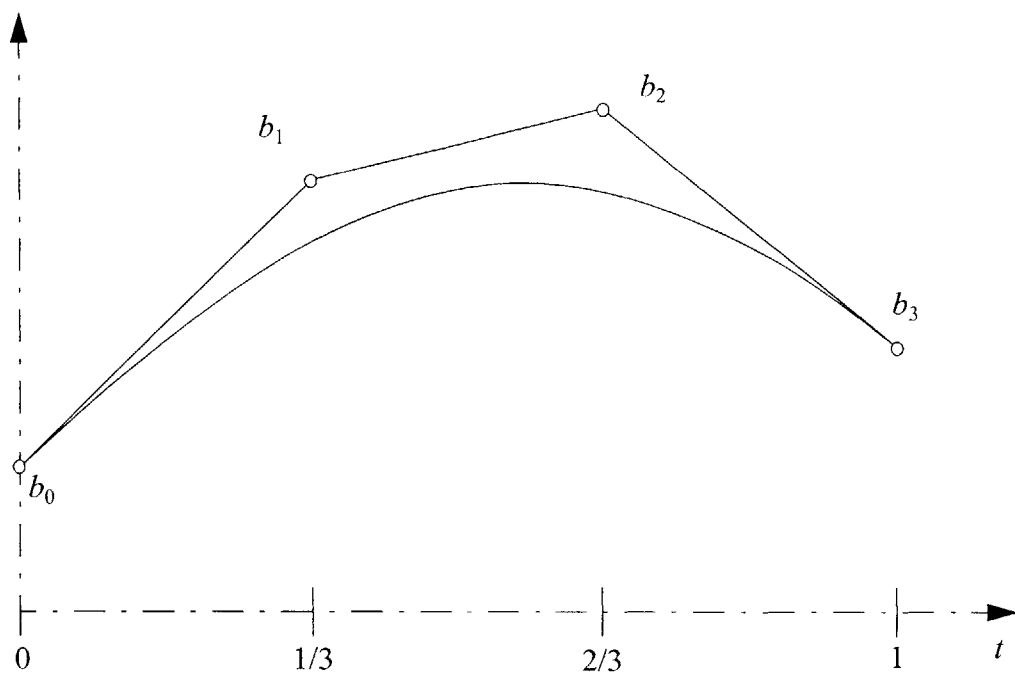


Fig. 3.3 A Bezier function.

The k -th derivative of a Bezier curve is given by

$$X^{(k)}(t) = \frac{n!}{(n-k)!} \sum_{i=0}^{n-k} \Delta^k \mathbf{b}_i B_i^{n-k}(t) \quad , \quad (3.4)$$

where Δk are forward difference operators defined as

$$\Delta \mathbf{b}_i \equiv \mathbf{b}_{i+1} - \mathbf{b}_i, \quad (3.5)$$

$$\Delta^2 \mathbf{b}_i \equiv \Delta(\Delta \mathbf{b}_i) = \Delta(\mathbf{b}_{i+1}, \mathbf{b}_i) = \mathbf{b}_{i+2} - 2\mathbf{b}_{i+1} + \mathbf{b}_i, \quad (3.6)$$

$$\Delta^k \mathbf{b}_i \equiv \sum_{l=0}^k (-1)^l \binom{k}{l} \mathbf{b}_{i+k-l}. \quad (3.7)$$

Important properties of Bezier curves are listed below:

- The Bezier curve begins and ends at \mathbf{b}_0 and \mathbf{b}_n , respectively.
- The edges $\overline{\mathbf{b}_0 \mathbf{b}_1}$ and $\overline{\mathbf{b}_{n-1} \mathbf{b}_n}$ of the Bezier polygon are tangent to the curve.
- The k -th derivative at the endpoint of a Bezier curve depends only on the boundary point and its k neighbors.

3.3 Bezier Surfaces and Related Functions

Bezier expansions can be formulated for two types of surface patches:

- *tensor-product* (four-sided)
- *triangular*

These are discussed in the following sections.

3.3.1 Tensor-product Bezier Surfaces and Functions

The surface geometry of a tensor-product Bezier patch is represented by the following relation:

$$\mathbf{X}(u,v) = \sum_{i=0}^n \sum_{k=0}^m \mathbf{b}_{ik} B_i^n(u) B_k^m(v) \quad (3.8)$$

where \mathbf{b}_{ik} are Bezier points distributed in three dimensional space and $u, v \in [0, 1]$. The Bezier points \mathbf{b}_{ik} comprise a three-dimensional Bezier net controlling the geometry of the patch. The Bezier net is analogous to the Bezier polygonal associated with Bezier curves. If the Bezier points are scalar-valued, then (3.8) is a function defined over the planar simplex, on which $u, v \in [0, 1]$, and a scalar distribution analogous to that shown for Bezier curves exists (see Fig. 3.3). In this case, the control points are referred to as Bezier ordinates (as for the Bezier curve).

The total number of Bezier control points \mathbf{b}_{ik} associated with a single QUAD panel is $(n_\phi + 1)(m_\phi + 1)$.

The partial derivatives of a tensor-product Bezier surfaces are given by:

$$\frac{\partial^r}{\partial u^r} \mathbf{X}(u, v) = \frac{n!}{(n-r)!} \sum_{i=0}^{n-r} \sum_{k=0}^m \Delta^{r0} \mathbf{b}_{ik} B_i^{n-r}(u) B_k^m(v) \quad , \quad (3.9)$$

$$\frac{\partial^s}{\partial v^s} \mathbf{X}(u, v) = \frac{m!}{(m-s)!} \sum_{i=0}^n \sum_{k=0}^{m-s} \Delta^{0s} \mathbf{b}_{ik} B_k^n(u) B_i^{m-s}(v) \quad , \quad (3.10)$$

where the forward differences are given by

$$\Delta^{r0} \mathbf{b}_{ik} = \Delta^{r-1,0} \mathbf{b}_{i+1,k} - \Delta^{r-1,0} \mathbf{b}_{ik} \quad \Delta^{0s} \mathbf{b}_{ik} = \Delta^{0,s-1} \mathbf{b}_{i,k+1} - \Delta^{0,s-1} \mathbf{b}_{ik} \quad . \quad (3.11)$$

For derivatives of a function, \mathbf{X} and \mathbf{b} in (3.9) to (3.11) are replaced by their scalar equivalents. Refer to [Hoschek 93] for further details.

3.3.2 Triangular Bezier Surfaces and Functions

A triangular Bezier surface is defined by the following parametric representation:

$$\mathbf{X}(\mathbf{u}) = \sum_{|\mathbf{I}|=n} \mathbf{b}_{\mathbf{I}} B_{\mathbf{I}}^n(\mathbf{u}), \quad (3.12)$$

where $B_{\mathbf{I}}^n(\mathbf{u})$ are the *generalized* Bernstein polynomials of degree n defined as

$$B_{\mathbf{I}}^n(\mathbf{u}) = B_{ijk}^n(\mathbf{u}) = \frac{n!}{i!j!k!} u^i v^j w^k, \quad (3.13)$$

and $\mathbf{b}_{\mathbf{I}}$ are control points (in 2-D or 3-D) that collectively form a Bezier net. In (3.12) and (3.13), \mathbf{I} is defined as $(i, j, k)^T$, with i, j , and k subject to the constraint $i + j + k = n$, with i, j , and k non-negative; \mathbf{u} is shorthand for $(u, v, w)^T$, the three barycentric coordinates with respect to a *base* triangle (planar), as shown in Fig. 3.4. For any point on the base triangle, the barycentric coordinates always sum to unity: $u + v + w = 1$, and the coordinates are non-negative.

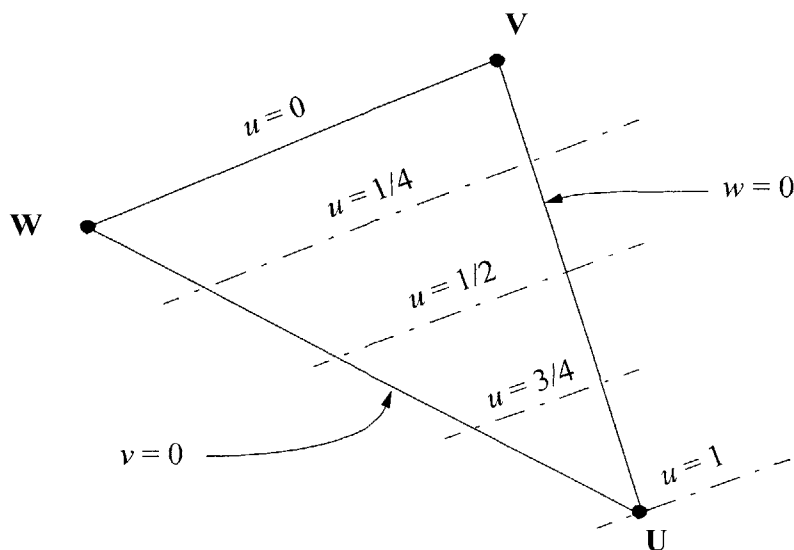


Fig. 3.4 Barycentric or area-based coordinates.

The vertices of the triangle are represented by upper-case **U**, **V**, and **W**, corresponding to $u = 1$, $v = 1$ and $w = 1$, respectively, so that any point on the planar triangle can be expressed as

$$\mathbf{P}(u, v, w) = u\mathbf{U} + v\mathbf{V} + w\mathbf{W}. \quad (3.14)$$

The barycentric coordinates are invariant under linear (affine) transformations. This property allows one to consider different shapes of the base triangle without affecting the Bezier patch itself.

The sum in (3.12) involves a total of $(n+1)(n+2)/2$ terms. For example, a triangular panel of degree 3 comprises 10 terms, yielding a three-dimensional Bezier net consisting of 10 Bezier points. For this case, the control point subscripts i, j, k are identified with the base triangle as shown in Fig. 3.5. Control points associated with the corner points of the base triangle are located on the actual vertices of the Bezier triangular patch.

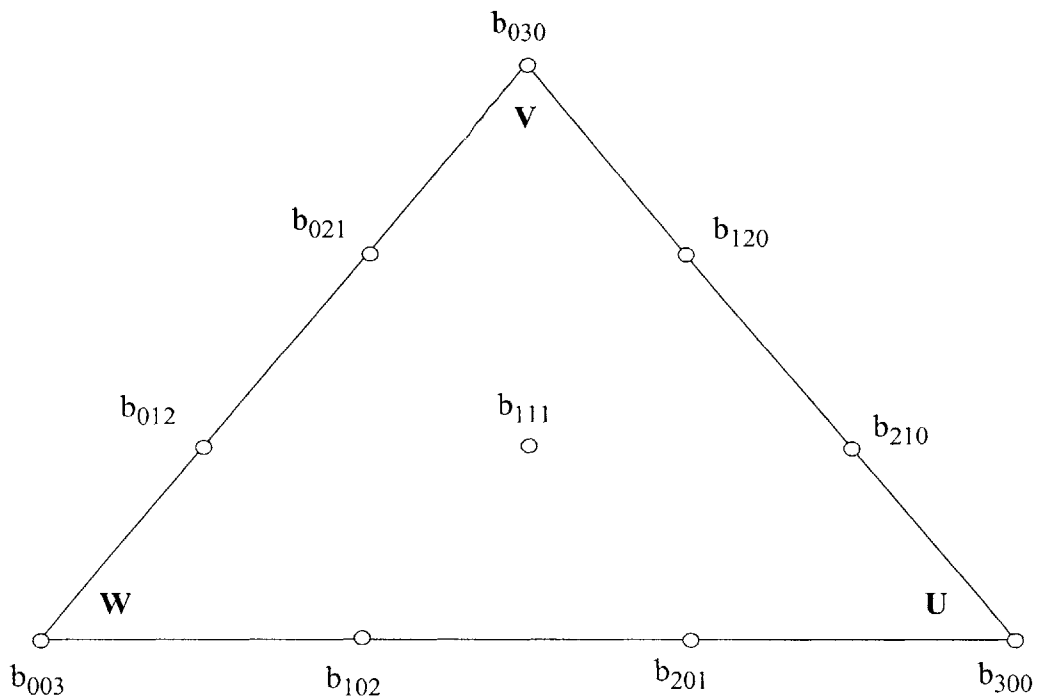


Fig. 3.5 Bezier control points associated with base triangle (case of $n = 3$).

If the control points in (3.12) are scalar-valued, the control points are referred to as Bezier ordinates (just as in the case of a Bezier curve). In this case, the Bezier ‘surface’ is a function defined over the base triangle, and the situation is analogous to that shown in Fig. 3.3 for the curve.

Derivatives on triangular Bezier patches cannot be expressed as partial derivatives, due to the constraint $u + v + w = 1$. However, derivatives can be expressed with respect to one of the parameters with the condition that one of the other parameters is held constant, e.g., see [Hoschek 93]:

$$\left. \frac{DX}{du} \right|_{v = \text{constant}} = n \sum_{i+j+k=n-1} (\mathbf{b}_{i+1,jk} - \mathbf{b}_{ij,k+1}) B_{ijk}^{n-1}(u, v, w) \quad (3.15)$$

$$\left. \frac{DX}{dv} \right|_{w = \text{constant}} = n \sum_{i+j+k=n-1} (\mathbf{b}_{i+1,jk} - \mathbf{b}_{i,j+1,k}) B_{ijk}^{n-1}(u, v, w) \quad (3.16)$$

$$\left. \frac{DX}{dw} \right|_{u = \text{constant}} = n \sum_{i+j+k=n-1} (\mathbf{b}_{i,j+1,k} - \mathbf{b}_{ij,k+1}) B_{ijk}^{n-1}(u, v, w) \quad (3.17)$$

For derivatives of a function, X and \mathbf{b} in (3.15) to (3.17) are replaced by their scalar equivalents.

Chapter 4

Bezier Based Higher Order Panel Method

This chapter presents the main elements of the Bezier-based higher-order panel method. The development of this method builds largely on previous chapters covering fundamentals of the boundary integral equation and Bezier representation of surfaces and functions.

4.1 Body and Wake Surface Discretization

Application of the method begins with a boundary mesh-generation process, whereby the surface of the body is decomposed into a set of unique, non-overlapping Bezier patches or *panels*. The collection of panels may comprise a combination of tensor-product Bezier surfaces and triangular Bezier surfaces, referred to here as QUAD and TRI panels, respectively. The wake boundary, when modeled explicitly, is partitioned in a similar manner (except that, as discussed in Chapter 2, only one side of an infinitesimally thin wake sheet is modeled).²⁰

A general requirement is that the interface between neighboring panels be continuous, i.e., C^0 continuity should exist at each such interface. Any gaps or ‘leakage’ between adjoining panels would likely have an adverse effect on the solution and therefore should be avoided. C^0 continuity is guaranteed by ensuring that adjoining panels share the same Bezier thread along the common edge, i.e., the Bezier points on that edge are common to both panels; this is true whether the interface between the two panels is QUAD-QUAD, TRI-TRI or QUAD-TRI.

The body boundary S_B is discretized into a total of N_B individual panels Λ_B^k such that

$$S_B = \bar{\Lambda}_B = \bigcup_{k=1}^{N_B} \bar{\Lambda}_B^k, \quad (4.1)$$

20. As discussed in Chapter 2, typically the wake boundary for non-lifting bodies is practically nonexistent. For a lifting body, the geometry of the wake sheet is given or assumed.

where the over-bar denotes closure (i.e., $\bar{\Lambda} = \Lambda + \partial\Lambda$). Similarly, an explicit wake boundary S_W is discretized into a total of N_W individual panels Λ_W^k satisfying

$$S_W = \bar{\Lambda}_W = \bigcup_{k=1}^{N_W} \bar{\Lambda}_W^k . \quad (4.2)$$

Conceptually, S_W is typically regarded as being semi-infinite in extent, however, as a practical matter, the number of panels in the wake is necessarily restricted to a finite quantity, as indicated in (4.2).²¹

The trailing edge of the body is defined as a closed curve formed by the intersection of the body and wake boundaries:

$$C_{TE} = \bar{\Lambda}_B \cap \bar{\Lambda}_W . \quad (4.3)$$

In a typical analysis of a lifting body, the trailing edge thickness is considered to be zero, in which case the area enclosed by C_{TE} approaches zero and the trailing edge resembles an open line or non-closed curve; despite any such appearance, however, the trailing edge must be treated as a closed curve if the body is to generate lift, as discussed in Chapter 2.

C^0 continuity between panels is ensured when the panels connect in a ‘simple’, conforming manner, so that

$$\bar{\Lambda}^i \cap \bar{\Lambda}^j = \text{an entire edge or an entire vertex of each panel} .^{22} \quad (4.4)$$

21. There are a number of ways in which this apparent dilemma is treated. For example, a semi-infinite line vortex can be used to emulate a ‘rolled-up’ wake sheet, as the potential induced by such a line vortex is known in closed form. For the propeller problem, see discussion in [Kerwin 78]. Details of the various approaches are beyond the scope of this thesis. One approach is simply to model the wake as a finite length sheet and rely on the fact that the influence of a normal dipole diminishes rapidly with distance from the body, on account of two effects. The potential induced at a field point on the body is 1) *inversely* proportional to the square of the distance between the field point and the point on the wake boundary, and 2) *proportional* to the dot product between the unit normal vector on the wake and the unit vector collinear with the field and wake points. The former obviously indicates a strong attenuating effect, and the latter tends to a low value for any field point on the blade, with increasing distance.

22. Cf. [Patera 95], in finite element context.

As mentioned, this condition is not difficult to achieve.

4.2 Bezier Modeling of Surface Geometry

The surface geometry of a QUAD panel is represented by the following tensor-product relation:

$$X(u,v) = \sum_{i=0}^n \sum_{j=0}^m \mathbf{b}_{ij} B_i^n(u) B_j^m(v) . \quad (4.5)$$

Typically, the degree of the Bezier polynomial corresponding to the parameter u is the same as that associated with the parameter v , in which case $n = m$; however, this is not a requirement. There may be panel configurations in which it is appropriate for n to differ from m .

A TRI-panel surface is defined by the following parametric representation:

$$X(\mathbf{u}) = \sum_{|\mathbf{l}|=n} \mathbf{b}_{\mathbf{l}} B_{\mathbf{l}}^n(\mathbf{u}) . \quad (4.6)$$

As discussed in the previous chapter, the above sum involves a total of $(n+1)(n+2)/2$ terms; for instance, a TRI panel of degree 3 comprises 10 terms, yielding a Bezier net consisting of 10 Bezier points. Also, \mathbf{u} is shorthand for (u, v, w) , the three barycentric coordinates, the sum of which is always unity: $u + v + w = 1$.

4.3 Bezier Modeling of Potential Distribution

The velocity potential distribution on a panel is modeled by means of a scalar Bezier function. The velocity potential over the entire body boundary is modeled using a collection of scalar Bezier patches. A one-to-one correspondence exists between the set of geometrical patches and the set of functional patches, so that each and every panel is characterized by a pair of unique Bezier expansions.

On any given panel, the scalar Bezier function is expressed in terms of a distribution of local potential ordinates $\{\hat{\phi}\}$ ('functional control points'). Each potential ordinate $\hat{\phi}$ is associated with a unique local node $\hat{\mathbf{x}}$ on the panel. For QUAD panels, the potential is given as

$$\Phi(u, v) = \sum_{i=0}^{n_\phi} \sum_{j=0}^{m_\phi} \hat{\phi}_{ij} B_i^{n_\phi}(u) B_j^{m_\phi}(v), \quad (4.7)$$

where degree n_ϕ and degree m_ϕ correspond to the u -wise and v -wise coordinate parameters, respectively. While n_ϕ and m_ϕ are analogous to n and m of the Bezier surface, there is no requirement that they be equal. Indeed, the Bezier potential patch and the Bezier surface patch are independent in this respect. The scalar Bezier ordinates $\hat{\phi}_{ij}$ comprise a Bezier net controlling the distribution of the potential over the QUAD panel and are analogous to the vector-valued Bezier points \mathbf{b}_{ij} which control the panel surface geometry. The total number of unknown potential ordinates $\hat{\phi}_{ij}$ associated with a single QUAD panel is $L_\phi^k = (n_\phi + 1)(m_\phi + 1)$; each potential ordinate is associated with a *local* panel node $\hat{\mathbf{x}}$, yielding a total of L_ϕ^k such nodes on the panel. The local panel nodes $\{\hat{\mathbf{x}}\}$ are three-dimensional position vectors corresponding to a *uniform* distribution of the panel coordinates (u, v) , where $u \in [0, 1]$, $v \in [0, 1]$, so that on any given panel, the nodes are unique, i.e., $\hat{\mathbf{x}}_i \neq \hat{\mathbf{x}}_j$ for $i \neq j$.

On TRI panels, the potential is given as

$$\Phi(\mathbf{u}) = \sum_{|I|=n_\phi} \hat{\phi}_I B_I^{n_\phi}(\mathbf{u}), \quad (4.8)$$

where $B_I^{n_\phi}(\mathbf{u})$ are the generalized Bernstein polynomials of degree n_ϕ . Again, n_ϕ is analogous to n , but there is no requirement that they be equal, and as with the QUAD panel, the triangular Bezier potential patch is independent from its Bezier surface patch, insofar as difference in degree is concerned. The scalar Bezier ordinates $\hat{\phi}_I$ comprise a Bezier net controlling the distribution of the potential over the TRI panel and are analogous to the vector-valued Bezier points \mathbf{b}_I which control the panel surface geometry. The total number of unknown potential ordinates ϕ associated with a single TRI panel is $L_\phi^k = (n_\phi + 1)(n_\phi + 2)/2$; each potential ordi-

nate ϕ is associated with a *local* panel node $\hat{\mathbf{x}}$, yielding a total of L_ϕ^k such nodes on the panel. The local panel nodes $\{\hat{\mathbf{x}}\}$ are three-dimensional position vectors corresponding to a uniform distribution of the TRI panel coordinates (u, v, w) , where $u \in [0, 1]$, $v \in [0, 1]$, $w \in [0, 1]$, subject to $u + v + w = 1$, so that on any given panel, the nodes are unique, i.e., $\hat{\mathbf{x}}_i \neq \hat{\mathbf{x}}_j$ for $i \neq j$.

It must be emphasized that the Bezier ordinates $\{\hat{\phi}\}$, and not the actual potential values $\{\Phi\}$, are the unknowns to be solved via the matrix equation. However, the matrix equation represents a global system of equations and therefore must be written in terms of *global* potential control points $\{\phi\}$. Each globally distinct Bezier ordinate ϕ is assigned as an element in the vector of unknowns. Once a matrix solution is obtained, the potential is computed thereafter using (4.7) or (4.8). Further details of the matrix equation are given in the sections to follow.

Although (4.7) and (4.8) are written using the symbol designated for the total potential Φ , the relations are valid for the perturbation potential as well.

It may be of interest to note that the triangular Bezier representation (4.8) has the same general form as expansions for unknown parameters commonly utilized in finite element analysis; the various types of finite element shape functions are analogous to the generalized Bernstein polynomials $B_I^{n_\phi}(\mathbf{u})$, as these are known weights factoring unknowns to be solved. In this regard, the tensor-product relation (4.7) fulfills the same role. For further details regarding finite element analysis, see, e.g., [Zienkiewicz 94]. An example of another weighting technique applied to potential flow integral equations is described by [Sclavounos 87], in which an averaging of the integral equation is performed in lieu of collocation (enforcement at a point).

4.4 The Discrete Form of the Boundary Integral Equation

Both the total potential and perturbation formulations are presented. Refer to Section 4.4.1 and 4.4.2, respectively.

4.4.1 Total Potential Formulation

The starting point is the boundary integral equation discussed in Chapter 2. The total potential formulation (2.22) is rearranged such that only known ‘loading’ terms reside on the right-hand side:

$$T\Phi(\mathbf{x}) + \iint_{S_B - S_e} \Phi(\xi) \frac{\partial G(\mathbf{x}; \xi)}{\partial n_\xi} d\xi + \iint_{\widehat{S}_w} \Delta\Phi(\xi_{TE}) \frac{\partial G(\mathbf{x}; \xi)}{\partial n_\xi} d\xi = \Phi_\infty(\mathbf{x}) \quad (4.9)$$

This boundary integral equation, which includes a term for the wake sheet, is discussed in further detail in [Kerwin 87] and [Lee 87]. For non-lifting bodies, the wake term is omitted.

At the discretization stage, field points are ordinarily located on the boundary and the coefficient T is therefore equal to $1/2$, provided the boundary is smooth. If the boundary is not smooth, then T is equal to the solid angle (in steradians) subtended at the field point by the boundary, divided by 4π . See, e.g., [Hunt 80]. Following the solution to (4.9), the potential may be computed at any other point in the domain Ω ; if \mathbf{x} lies within the domain but not on the boundary $\partial\Omega$, then T takes on a value of 1 .

In the following discussion, the field point \mathbf{x} is assumed to be fixed, so that only one *instance* of (4.9) is under consideration; in other words, only a single row of the influence matrix is being considered. In addition, T is assumed to be known (say, $T = 1/2$). The first step in obtaining a discrete form of (4.9) is to partition the region of integration of each boundary integral in (4.9) in direct correspondence with the panel arrangement, i.e., the first integral according to the set of body panels $\{\Lambda_B^k\}$ and the second according to the set of wake panels $\{\Lambda_w^k\}$:

$$T\Phi(\mathbf{x}) + \sum_{k=1}^{N_B} \iint_{\Lambda_B^k} \Phi(\xi) \frac{\partial G(\mathbf{x}; \xi)}{\partial n_\xi} d\xi + \sum_{k=1}^{N_w} \iint_{\Lambda_w^k} \Delta\Phi(\xi_{TE}) \frac{\partial G(\mathbf{x}; \xi)}{\partial n_\xi} d\xi = \Phi_\infty(\mathbf{x}). \quad (4.10)$$

Before proceeding further it is necessary to consider the nature of the matrix equation to be assembled. The prototype implementation of this panel method employs a non-overdetermined system of equations of the following form:

$$\mathbf{A} \cdot \boldsymbol{\varphi} = \mathbf{c} \quad (4.11)$$

where \mathbf{A} is a square *influence matrix*, $\boldsymbol{\varphi}$ is a vector of unknown potential ordinates, and \mathbf{c} is a vector of known ‘loads’. The size of $\boldsymbol{\varphi}$ corresponds to a total of M globally unique nodes $\{\mathbf{x}\} = \{\mathbf{x}_1, \dots, \mathbf{x}_M\}$ associated with the body boundary panels Λ_B^k . In general, $\mathbf{x}_i^\varphi \neq \mathbf{x}_j^\varphi$ for $i \neq j$, however in the case of a zero-thickness trailing edge, a pair of nodes associated with panels on the ‘upper’ and ‘lower’ sides of S_B respectively and lying on C_{TE} may ‘legitimately’ occupy the same physical location. At a zero-thickness trailing edge of a lifting foil, therefore, uniqueness of a global node is not established exclusively by position; when ambiguity of position occurs on C_{TE} , uniqueness is determined by distinguishing between panels *attached* to the node in question. For all nodes not on C_{TE} , however, uniqueness of nodal position *is* sufficient to establish uniqueness of a global node.

A one-to-one correspondence exists between the global nodes $\{\mathbf{x}\}$ and the global potential ordinates $\{\varphi\}$. The global nodes $\{\mathbf{x}\}$ are usually referred to as ‘field points’, particularly when used as an argument in the boundary integral equation. However, a global node is not necessarily a field point *per se*, as the matrix equation may incorporate one or more auxiliary equations in lieu of the boundary integral equation, as discussed in Section 4.8.

To facilitate dissection of (4.10), it is useful to establish two mapping systems, g and h , for use in conjunction with body and wake panels, respectively. The main purpose of these mappings is to establish linkage between the local potential ordinates $\{\hat{\varphi}\}$ and the global potential ordinates $\{\varphi\}$. *These mappings are nothing more than a bookkeeping system to facilitate assembly of the matrix equation, which requires some method of specifying which columns of the influence matrix are to be ‘entered’ into.* Following along the lines of [Patera 95], a panel-to-global mapping g_j^k for body panels is introduced: $\forall k \in \{1, \dots, N_B\}$, $\forall j \in \{1, \dots, L_\varphi^k\}$, there exists an $i = g_j^k$ such that $\mathbf{x}_i = \hat{\mathbf{x}}_j^k$ and $\varphi_i = \hat{\varphi}_j^k$, where the $\hat{\mathbf{x}}_j^k$ are the local panel nodes

and $\hat{\phi}_j^k$ are the local potential ordinates on the body panels Λ_B^k . Thus, the body panel mapping g_j^k also serves to associate local panel nodes $\{\hat{\mathbf{x}}\}$ with global nodes $\{\mathbf{x}\}$.

To evaluate the integral over the wake boundary, it is necessary to associate the potential on any given wake panel with the potential at the trailing edge of the body, and for this purpose, a panel-to-global mapping h_{jl}^k for wake panels is introduced: $\forall k \in \{1, \dots, N_w\}$, $\forall j \in \{1, \dots, L_\phi^k\}$ and $\forall l \in \{1, 2\}$, there exists an $i = h_{jl}^k$ such that $\phi_i = \hat{\phi}_{jl}^k$, where the $\hat{\phi}_{jl}^k$ are the local potential ordinates on the wake panels. For this mapping, i will always map to a global control point at the trailing edge. The additional subscript l is necessary in order to denote the ‘side’ of the foil (e.g., $l = 1$ and $l = 2$ correspond to the ‘lower’ and ‘upper’ sides of the blade, respectively). Unlike the body panel-to-global mapping, the wake panel-to-global mapping h_{jl}^k is a ‘one-to-many’ mapping.

With these mappings at our disposal, the r -th row of the influence matrix \mathbf{A} can be reduced to the following (colon notation is used, e.g., see [Golub 96]):

$$\mathbf{A}(r, :) = \sum_{k=1}^{N_B} \sum_{j=1}^{L_\phi^k} \mathbf{A}^B(r, g_j^k) + \sum_{k=1}^{N_w} \sum_{j=1}^{L_\phi^k} \sum_{l=1}^2 \mathbf{A}^W(r, h_{jl}^k), \quad (4.12)$$

where r corresponds to a single field point \mathbf{x} (global node), and matrices \mathbf{A}^B and \mathbf{A}^W are defined as

$$\mathbf{A}^B(r, g_j^k) = T \delta_{r g_j^k} + \mathbf{D}_j^k, \quad (4.13)$$

$$\mathbf{A}^W(r, h_{jl}^k) = (-1)^l \mathbf{D}_j^k. \quad (4.14)$$

In (4.13), $\delta_{r g_j^k}$ is the Kronecker delta, which is unity when $r = g_j^k$, and zero otherwise. The row vector \mathbf{D} is composed of four prime ingredients:

- Kernel
- Potential distribution represented by Bezier scalar function (shape function)

- Jacobian to transform domain of integration from 3-D panel to 2-D simplex
- Quadrature weights

Before examining the details of the row vector \mathbf{D} , it is worthwhile to put \mathbf{D} into perspective by observing that the multiplication of \mathbf{D} by the vector of potential control points on a given panel yields the potential induced at a field point \mathbf{x} due to a normal-dipole distribution over that panel, with dipole strength corresponding to the values of the potential control points $\{\hat{\phi}\}$:

$$\Phi(\mathbf{x})_{\text{INDUCED BY A SINGLE PANEL}} = \mathbf{D} \cdot \hat{\phi} = \begin{bmatrix} D_1 & D_2 & \dots & D_{L_\varphi} \end{bmatrix} \begin{bmatrix} \hat{\phi}_1 \\ \hat{\phi}_2 \\ \dots \\ \hat{\phi}_{L_\varphi} \end{bmatrix} \quad (4.15)$$

Recall that L_φ^k is the quantity of potential control points over the panel given by index k . Now compare (4.15) with (4.7) or (4.8) and it is seen that the Bernstein polynomials are contained in \mathbf{D} . The key is to construct \mathbf{D} in such a way that (4.7) and (4.8) is ‘recovered’ for a QUAD and TRI panel, respectively. Note that (4.15) is really the contribution from a single panel to the first integral in the boundary integral equation (4.10).

Referring back to the four components of \mathbf{D} listed above, the kernel is equivalent to a normal dipole, cf. (2.20), distributed on the boundary with strength related to the value of potential represented by the Bezier scalar function, (4.7) and (4.8) for QUAD and TRI panels, respectively. Provided the panel is smooth and a one-to-one mapping from the three-dimensional panel domain onto a domain of the (u, v) -plane exists, integration over the panel can be carried out conveniently by use of Jacobian determinants which give the differential area of the panel in terms of the local panel coordinates u and v , as follows (see, e.g., [Zienkiewicz 94]):

$$dS = \begin{bmatrix} \frac{\partial x}{\partial u} \\ \frac{\partial y}{\partial u} \\ \frac{\partial z}{\partial u} \end{bmatrix} \times \begin{bmatrix} \frac{\partial x}{\partial v} \\ \frac{\partial y}{\partial v} \\ \frac{\partial z}{\partial v} \end{bmatrix} du dv \quad (4.16)$$

Quadrature weights associated with integration points depend on the order of integration as well as the type of integration rule. This is discussed further below and in sections to follow.

Combining the elements mentioned above, an element j of the row vector \mathbf{D} associated with a given panel (index k) and field point \mathbf{x} may be expressed in the following form:

$$\mathbf{D}_j^k(\mathbf{x}) = \sum_{q=1}^{N_Q} B_{jq} K_q(\mathbf{x}) J_q Q_q \quad j \in \{1, \dots, L_\phi^k\}. \quad (4.17)$$

All four components inside the quadrature summation in (4.17) depend on the quadrature point given by index q , and of which there are a total of N_Q . The only component having any dependence on \mathbf{x} is K_q , which is nothing more than the kernel given by (2.20), with the source point corresponding to the quadrature point q . It should be noted that even though quadrature is being performed over a 2-D simplex (unit square in first quadrant for QUAD panels, unit right triangle for TRI panels), where for square or rectangular domains it is typical to perform quadrature using a pair of summations (one nested inside the other), the quadrature is easily converted to a single index summation, i.e., the form used in (4.17).

In (4.17), J_q is given by the cross-product in (4.16). The quadrature weight factor Q_q is given as

$$Q_q = \begin{cases} \frac{(W_i W_j)_q}{4} & \text{QUAD panel} \\ \frac{(W_\Delta)_q}{2} & \text{TRI panel} \end{cases} \quad (4.18)$$

where W_i and W_j are Gauss-Legendre quadrature weights corresponding to abscissae (integration nodes or offsets) in the open interval $(-1, 1)$, and W_Δ are Gaussian weights given by [Cowper 73]. Values of the weights and abscissae for the QUAD case are given in many engineering texts, and also can be easily computed; see, e.g., [Press 92]. Quadrature is discussed further in Sections 4.4 and 4.5. The divide-by-4 shown for QUAD panels is required when the integration is performed in the first-quadrant, i.e., $0 < u, v < 1$, while using quadrature weights corresponding to the interval $(-1, 1)$. This requires a simple transformation given in [Mohr 92]:

$$u_i = 0.5(1 - a_i) \tag{4.19}$$

where a_i is the quadrature abscissa in the interval $(-1, 1)$ and u_i (or v_i) is the resulting parameter in the interval $(0, 1)$. Integrating in the interval $(0, 1)$ is convenient with respect to the typical range of parameters (u, v) used in Bezier tensor-product patches, i.e., $(0, 1)$. For TRI panels, the integration is performed over a unit triangle with area = $1/2$, which is precisely the divide-by-2 factor shown in (4.18).

Last but certainly not least, B_{jq} is obtained by deconstructing or ‘reverse engineering’ (4.7) or (4.8). For QUAD panels, each B_{jq} involves a single product of two Bernstein components $B_i(u) B_j(v)$,²³ while for TRI panels, each B_{jq} is simply a single value of $B_f(u, v, w)$.

The element in the load vector \mathbf{c} is simply the value of the incident potential at the field point, cf. (4.9) and (4.11).

Assembly of the matrix equation is discussed further in Section 4.8.

4.4.2 Perturbation Potential Formulation

Referring to Chapter 2, the boundary integral equation for the perturbation potential is

23. The subscript j in $B_i(u)B_j(v)$ is not to be confused with the subscript j in B_{jq} . The former j is associated with the summation over the potential control points on a panel (cf. Equation. 4.7), while the latter j is an index referring to the element of the row vector \mathbf{D} .

$$T\phi(\mathbf{x}) + \iint_{S_B - S_\epsilon} \phi(\xi) \frac{\partial G(\mathbf{x}; \xi)}{\partial n_\xi} d\xi + \iint_{\widehat{S}_w} \Delta\phi(\xi_{TE}) \frac{\partial G(\mathbf{x}; \xi)}{\partial n_\xi} d\xi = \iint_{S_B - S_\epsilon} G(\mathbf{x}; \xi) \frac{\partial \phi(\xi)}{\partial n_\xi} d\xi. \quad (4.20)$$

The above equation is arranged with all known terms (‘loads’) on the right-hand side. As the left-hand side is identical in form to that of the total potential formulation (4.9), the procedure for assembling the influence matrix is identical to that described in Section 4.4.1; furthermore, the load vector \mathbf{c} in the matrix equation is assembled by straightforward extension of techniques described in that section.

4.5 Avoiding Singularity Problems in the Induction Integrals

From a computational standpoint, it is clear that any ‘encounters’ with singularities must be avoided. As discussed in Chapter 2, the boundary integral equations contain singular kernels, which must be considered in the implementation of the numerical integration procedures. The singularity originates from Green’s function (2.15), and the gradient of Green’s function (2.20), both of which contain a distance parameter r in the denominator. Both the ‘source term’ (integral whose integrand is proportional to G) and the ‘dipole’ term (integral with integrand proportional to $\frac{\partial G}{\partial n}$) are singular, as the kernels approach infinity as r approaches zero (i.e., as the field point \mathbf{x} approaches the source point ξ). Moreover, the kernels are strongly singular, since r is raised to a power greater than or equal to unity.

Whereas the kernels in (4.9) and (4.20) are singular in behavior, the area of integration *excludes* an infinitesimally small region S_ϵ surrounding the field point, so that, in principle, a singularity is not encountered within the region of integration.²⁴ The form of the integral equation, as derived, is such that the region S_ϵ has already been accounted for; the value attributed to the integration over S_ϵ is contained in the ‘free’ potential term, i.e., the first term in (4.9) or (4.20). While these boundary integral equations are effectively non-singular, due consideration to the singular nature of the kernels must be given. In choosing a numerical integration procedure, at least two basic requirements come to mind:

24. The region of integration may be compared to a surface having a pin-hole at the location of the field point.

1. The procedure must avoid divide-by-zero errors and associated solution inaccuracies;
2. The ‘free’ potential value corresponding to S_ϵ must not be duplicated (no ‘double dipping’), as the contribution to the integral has already been evaluated in the process of de-singularizing the integral equation. See Section 2.2.

The numerical integration strategy employed in the prototype implementation is relatively straightforward. Gauss-Legendre quadrature is utilized, with one basic restriction imposed: *A field point must not be present within the perimeter of the quadrature domain.* A field point may, however, be present *on* the perimeter of the quadrature domain. This guideline follows from the two characteristics of Gauss-Legendre quadrature (see, e.g., [Funaro 92]):

- a.* The Gauss-Legendre abscissae never occur on the perimeter of the quadrature domain, since it is an open type quadrature rule. As the quadrature order increases, the ‘outermost’ Gauss abscissae approach the perimeter, but never reach it.
- b.* As the order of quadrature increases, the weight values associated with the outermost Gauss abscissae approach zero.

Accordingly, it is hypothesized that Requirements 1 and 2 are satisfied when employing Gauss-Legendre quadrature, subject to the restriction that the field points lie on or outside the quadrature perimeter, but not inside. It may be noted that Characteristics *a* and *b* more or less correspond to Requirements 1 and 2, respectively.

Remark: In utilizing Gauss-Legendre quadrature to compute the boundary integrals in (4.9) or (4.20), it appears that the Cauchy principal value (cf. footnote 16) is automatically obtained, thus satisfying Requirement No. 2 above. This statement is based on results obtained from the single-panel quadrature tests described in Section 4.6.

It turns out that Gauss-Legendre quadrature is generally not the most accurate means of integrating the boundary element kernels (for a given number of integration points). Various other methods have appeared in the literature in the past 15-20 years, e.g., 1) weighted Gaussian, 2) triangle-square regularizing transformation, and 3) series expansion combined with singularity subtraction. See, e.g., [Lean 85] and [Aliabadi 89]. However, this finding does not necessarily mean that standard Gauss-Legendre quadrature is not useful for this purpose, particularly when a stable, accurate and consistent means of modeling the geometry is available. Critical to the determination of the boundary integrals is the computational quality of the geo-

metrical coordinates, derivatives and Jacobians. On any given panel, the Bezier representation provides an extremely smooth and stable representation of the geometry; in addition, it is a relatively simple matter to ensure fully conforming inter-panel connections, i.e., C^0 continuity.

For discussion purposes it is convenient to establish a simple classification system for field point location, with respect to a given panel, as follows:

- EXTERIOR: A field point that is not contiguous with the panel.
- EDGE: A field point that lies on an edge, but not vertex, of the panel.
- VERTEX: A field point that lies on a vertex (corner) of the panel.
- INTERIOR: A field point that lies on the panel, within the panel perimeter.

When an integration must be performed for an INTERIOR-type field point, a subdivision of quadrature domains ('quadrature subdomains') on the panel is utilized to facilitate integration. The method of subdivision used in the prototype implementation comprises a uniform subdivision of the panel in parameter space u, v . The quantity of 'subdomains' is therefore given by:

$$\text{Number of Quadrature Subdomains on Panel} = \begin{cases} n_\phi m_\phi & \text{QUAD panel} \\ n_\phi^2 & \text{TRI panel} \end{cases} \quad (4.21)$$

4.6 Quadrature Tests

Gauss-Legendre quadrature is probably the most extensively used *open* type integration rule in engineering analysis. However, there appears to be a fair amount of controversy as regards its applicability to boundary element methods, particularly with respect to integration over a panel on which a field point (singularity) is present.

In order to obtain a quantitative measure of performance of conventional Gauss-Legendre quadrature as applied to the Bezier-based panel method, several quadrature tests were performed. Each test comprises a single panel, and the objective is to compute, using standard Gauss-Legendre quadrature, the potential induced by a constant-strength source distribution

and a constant-strength normal dipole distribution over the panel. The test “field point” (for which the induced potential is computed) is typically located at one of the vertices of the panel. In any case, the field point is never permitted to lie in the interior of the quadrature domain, so when a field point is located within the perimeter of a panel, a subdivision of the panel exists to facilitate integration, cf. (4.21). The computation of the induced potential is repeated with progressively increasing quadrature order. Panel aspect ratio and size were varied in some of the tests.

A further purpose of these tests is to establish a baseline performance benchmark for comparison with other methods at a later date. In addition, the tests were performed with the hope of gaining a better grasp of any limitations inherent in standard Gauss-Legendre quadrature as applied to the problem under consideration.

The battery of quadrature tests is summarized in Table 4.1. For each listing, two separate computations were performed, corresponding to 1) a unit source distributed over the panel, and 2) a unit normal dipole distributed over the panel.

Table 4.1 - Summary of single-panel quadrature tests.

Panel Type	Form	Subdivided?	Field Point Location
QUAD	planar	NO	VERTEX
QUAD	planar	YES	VERTEX
QUAD	spherical	NO	VERTEX
QUAD	spherical	YES	VERTEX
TRI	planar	NO	VERTEX
TRI	planar	YES	VERTEX
TRI	spherical	NO	VERTEX
TRI	spherical	YES	VERTEX

The potential induced at a field point \mathbf{x} due to a unit-strength source distributed over a panel Λ is

$$\Phi^S = - \int_{\Lambda} \frac{1}{4\pi|\mathbf{x} - \boldsymbol{\xi}|} d\xi, \quad (4.22)$$

while the potential induced at a field point \mathbf{x} due to a unit-strength dipole distributed over a panel Λ is

$$\Phi^D = - \int_{\Lambda} \frac{(\mathbf{x} - \boldsymbol{\xi}) \cdot \mathbf{n}(\boldsymbol{\xi})}{4\pi|\mathbf{x} - \boldsymbol{\xi}|^3} d\xi \quad (4.23)$$

Equations (4.22) and (4.23) are numerically integrated as discussed in previous sections.

Referring to the unit square planar QUAD panel shown in Fig. 4.1, it can be shown that the exact induced potential at the corner field point due to a unit source distribution is:

$$\Phi^S = \frac{\ln(1 + \sqrt{2})}{2\pi}, \quad (4.24)$$

while the corresponding value for a dipole distribution is zero. For the unit planar TRI panel shown in Fig. 4.2, the exact value of the induced potential at the same field point due to a unit-strength source distribution is simply one half the value given in (4.24)

For the spherical QUAD panel shown in Fig. 4.3, it can be shown that the exact value of potential induced at the field point, by a unit-strength source distribution, is

$$\Phi^S = -\frac{1}{2\pi} \sin(|\theta|) \ln\left(\tan\left(\frac{3\pi}{8}\right)\right), \quad (4.25)$$

while the potential due to a unit-strength dipole is exactly one half the value given in (4.25).

For the spherical TRI panel shown in shown in Fig. 4.4, the exact value of potential induced by a unit-strength source distribution is

$$\Phi^S = -\frac{R|\alpha|}{2\pi} \sin\left(\frac{|\theta|}{2}\right). \quad (4.26)$$

Again, the potential induced by a unit-strength normal dipole distribution is exactly one half that given in (4.25).

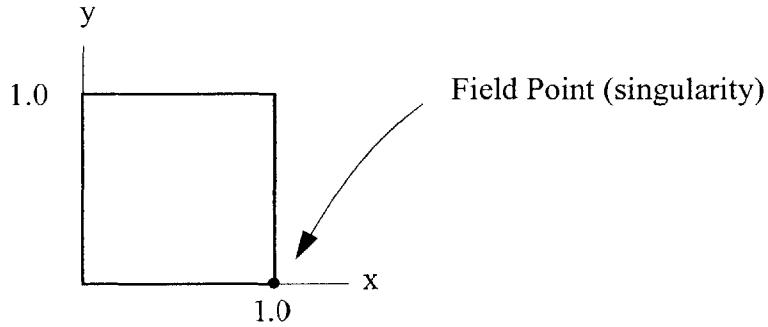


Fig 4.1 Domain of unit planar QUAD panel used in single-panel quadrature test.

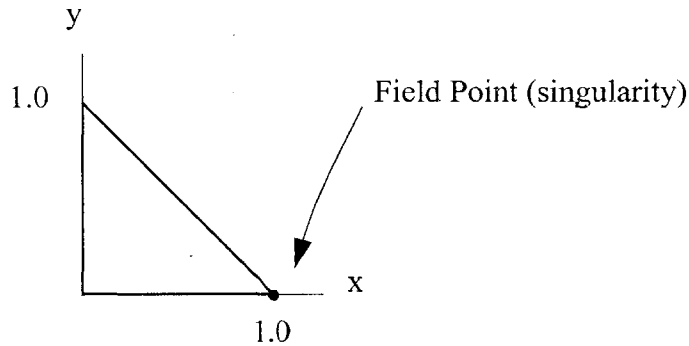


Fig 4.2 Domain of unit planar TRI panel used in single-panel quadrature test.

The computed values of induced potential have been compared with the exact values obtained from the relations discussed above. Most of these comparisons are shown in Fig.'s 4.5 to 4.8.

A sampling of error results for the spherical TRI panel is shown in Tables 4.2a, 4.2b and 4.2c. These results correspond to integration *without* subdividing the panel into multiple

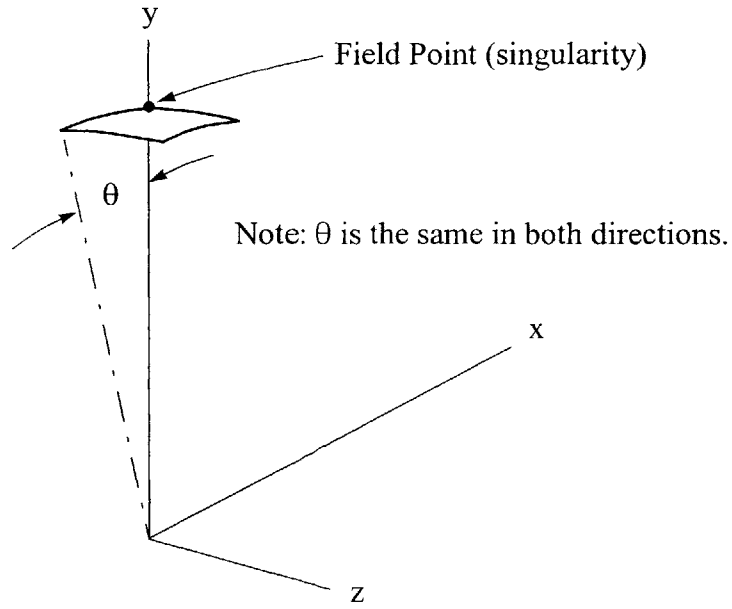


Fig 4.3 Domain of spherical QUAD panel used in single-panel quadrature test.

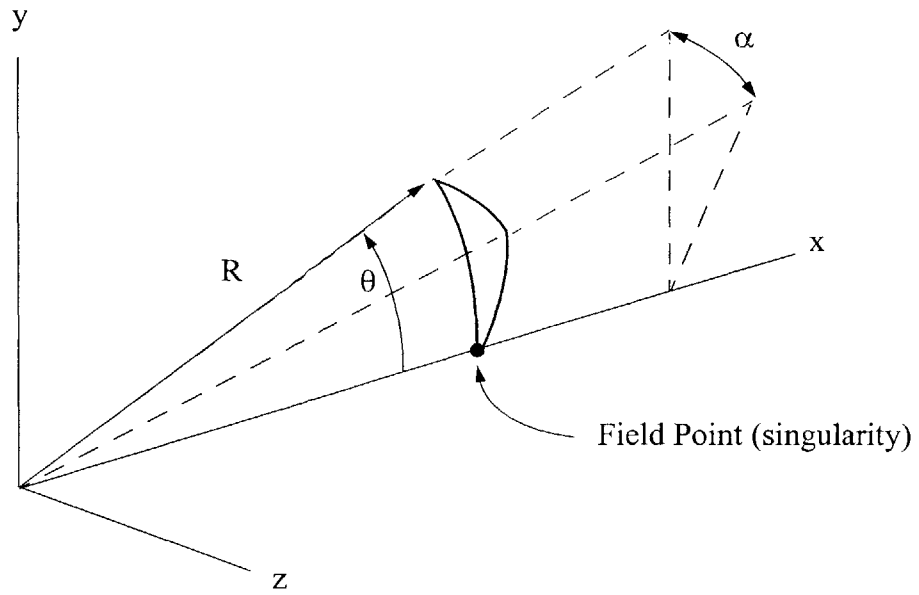


Fig 4.4 Domain of spherical TRI panel used in single-panel quadrature test.

quadrature subdomains. Referring to Fig. 4.4, the results listed in Table 4.2a are for θ fixed at 0.1 degrees, with various values of α ranging from 0.1 to 90 degrees. In Table 4.2b, α is fixed at 0.1 degrees, while θ is varied in a range from 0.1 to 90 degrees. In Table 4.2c, both θ and α are varied from 1 to 90 degrees.

Based on these tests several observations can be made:

- In many cases, the error associated with the source distribution is nearly identical to that of the dipole distribution.
- For planar panels, the error is independent of panel size, and all the source-test errors are negative, i.e., $\left| \frac{\Phi_{\text{CALC}}}{\Phi_{\text{EXACT}}} \right| < 1$. The absolute value of the source-test errors decrease with increasing quadrature order. The dipole-test errors compute to zero to within machine accuracy.
- For spherical panels, the error decreases with increasing quadrature order, provided the solid angle (in steradians) is not ‘too large’. As the solid angle increases, some point is reached when the sign of the error changes. As seen in Fig. 4.8, the sign of the error for spherical QUAD panels changes from negative to positive as the solid angle increases, as indicated by the rapid change in the curve.
- For TRI panels, the error does not increase significantly with increasing aspect ratio (ratio of α to θ), even for very large aspect ratios, provided that α or θ is not ‘too large’.

One salient difference between QUAD and TRI panels is the means by which quadrature weights and abscissae are obtained. For QUAD panels, algorithms exist for this purpose, for practically unlimited order of quadrature; e.g., see [Press 92]. As far as the author is aware, no such algorithms exist for triangular domains, at least for the symmetrical Gaussian formulae of the Hammer and co-workers type given in [Cowper 73]; the highest-order formula provided in that reference corresponds to the 13-point integration rule. According to Cowper, the discovery of additional formulas “remains a matter of *ad hoc* investigation”. There is the possibility that additional formulae have been introduced since Cowper’s publication 28 years ago. In any case, alternate quadrature methods exist for triangular domains; see, e.g., [Mohr 92].

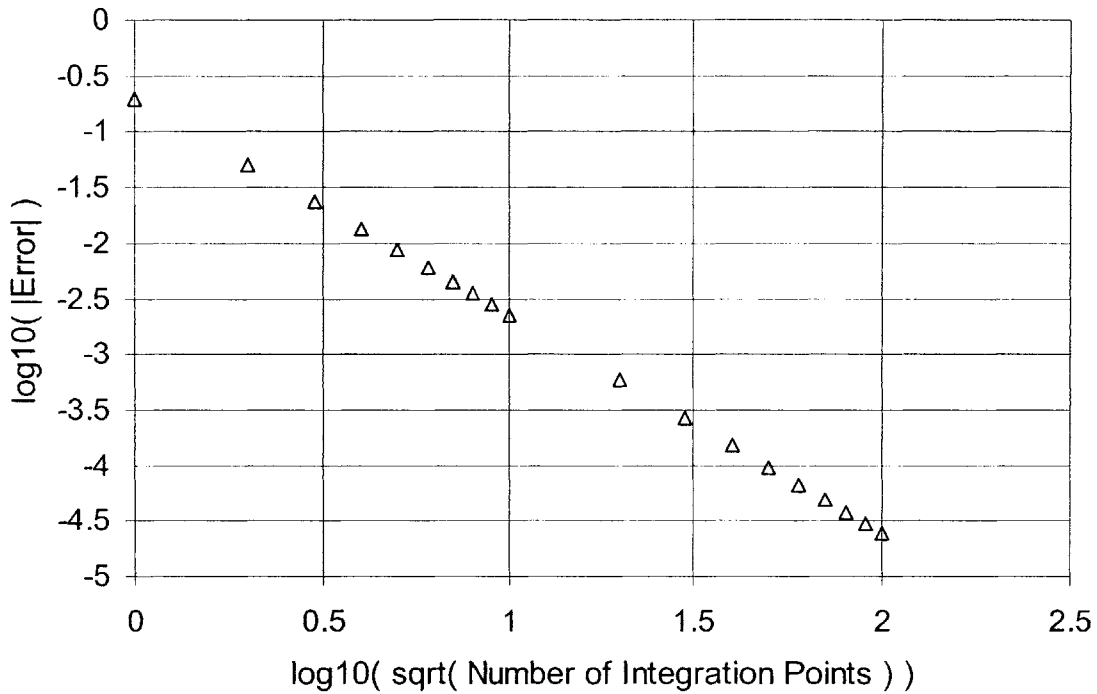


Fig. 4.5

Errors using standard Gauss-Legendre quadrature in computation of the potential induced by a constant-strength source distribution over a *planar* square-shaped QUAD patch, with singularity (field point) located at a corner node (see Fig. 4.1). Error is independent of patch size and degree of Bezier surface.

No error occurs in the computation of the potential induced by a constant-strength normal dipole; the computed value agrees with the exact value (identically zero in this case).

Note: The abscissa can be misleading. The number of integration points corresponding to several values of the abscissa are:

$\log_{10}(\sqrt{\text{Number of Integration Points}})$	Number of Integration Points
0	1
0.25	~3
0.5	10
1.0	100
1.5	1000
2.0	10000

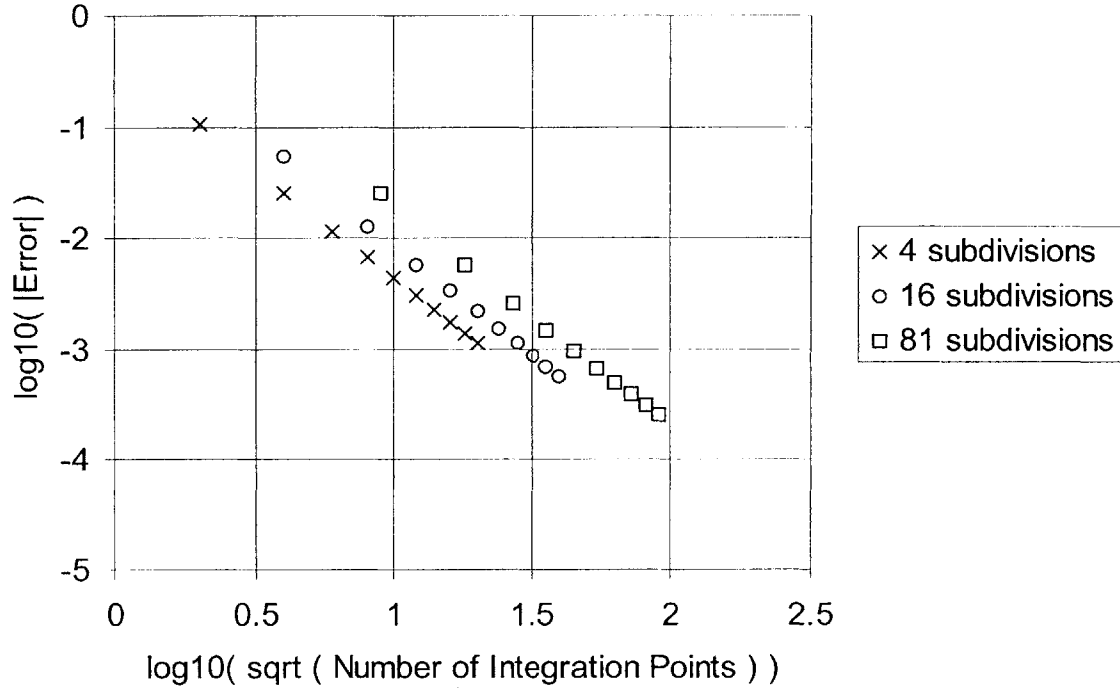


Fig. 4.6

Error using standard Gauss-Legendre quadrature in computation of the potential induced by a constant-strength source distribution over a *planar* square-shaped QUAD patch, with singularity (field point) located at a corner node (see Fig. 4.1). Patch is subdivided into separate equally-sized quadrature domains, as indicated. Error is independent of patch size and degree of Bezier surface.

No error occurs in the computation of the potential induced by a constant-strength normal dipole; the computed value agrees with the exact value (identically zero in this case).

Note: The abscissa can be misleading. The number of integration points corresponding to several values of the abscissa are:

log10 (sqrt (Number of Integration Points))	Number of Integration Points
0.25	~3
0.5	10
1.0	100
1.5	1000
2.0	10000

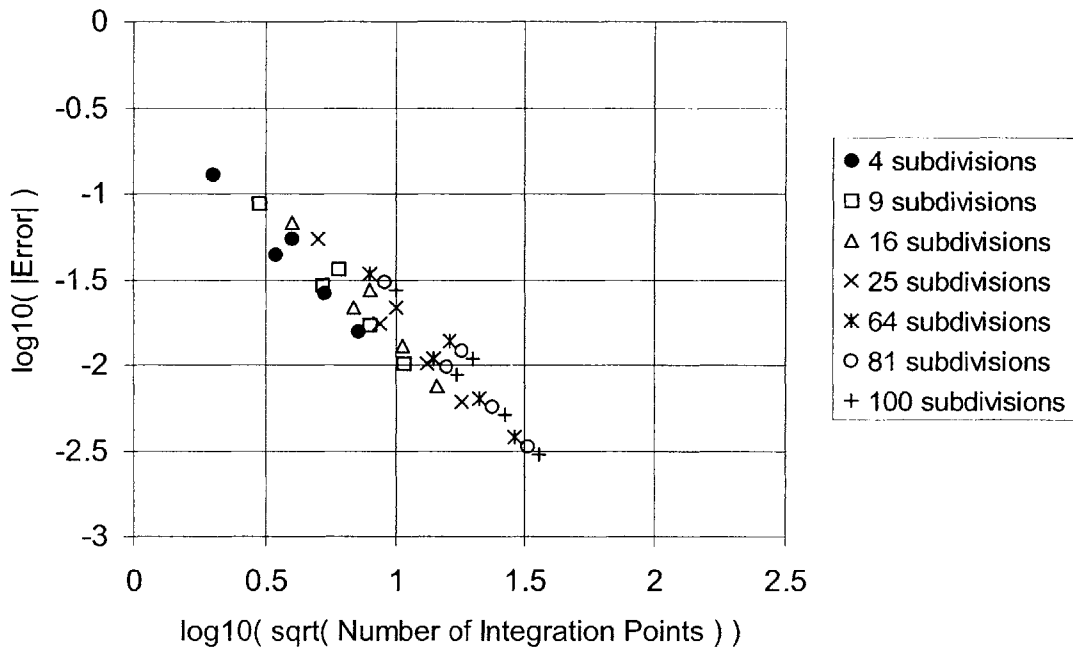


Fig. 4.7

Error using standard Gauss-Legendre quadrature in computation of the potential induced by a constant-strength source distribution over a *planar* TRI patch, with singularity (field point) located at a vertex node (see Fig. 4.2). Patch is subdivided into separate equally-sized quadrature domains, as indicated. Error is independent of patch size and degree of Bezier surface.

No error occurs in the computation of the potential induced by a constant-strength normal dipole; the computed value agrees with the exact value (identically zero in this case)

Note: The abscissa can be misleading. The number of integration points corresponding to several values of the abscissa are:

log10 (sqrt (Number of Integration Points))	Number of Integration Points
0.25	~3
0.5	10
1.0	100
1.5	1000
2.0	10000

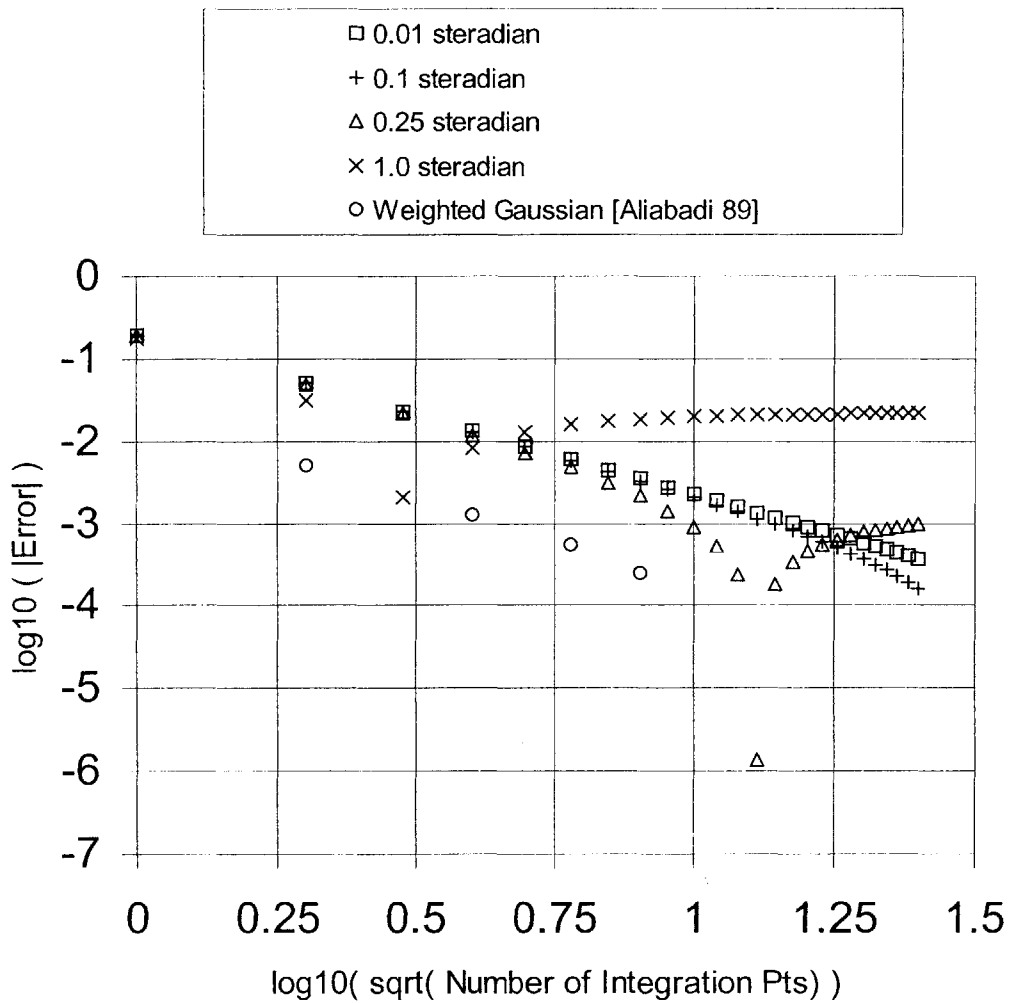


Fig. 4.8

Errors using standard Gauss-Legendre quadrature in computation of potential induced by constant-strength source distribution over a *spherical* QUAD patch, with field point (singularity) located at a corner node (see Fig. 4.3). Patch is Bezier surface of degree 4, varying in size (in terms of solid angle) as shown. Results are essentially unchanged for the potential induced by a constant-strength normal dipole.

Results from [Aliabadi 89] using *weighted* Gaussian integration are shown for comparison.

Note: The abscissa can be misleading. The number of integration points corresponding to several values of the abscissa are:

$\log_{10}(\text{sqrt}(\text{Number of Integration Points}))$	Number of Integration Points
0	1
0.25	~3
0.5	10
1.0	100
1.5	1000

Table 4.2a Quadrature test errors (in percent) for *spherical* TRI panel, with $\theta = 0.1$ degree and various α .

Num PTS	$\alpha = 0.1$		$\alpha = 1$		$\alpha = 5$		$\alpha = 30$		$\alpha = 60$		$\alpha = 90$	
	S	D	S	D	S	D	S	D	S	D	S	D
1	25.00	25.00	25.00	25.00	24.99	25.04	24.63	26.32	23.65	30.11	22.42	35.92
3	10.00	10.00	10.00	10.00	9.99	10.01	9.59	10.26	8.32	11.32	6.04	13.97
4	11.98	11.98	11.98	11.98	11.97	11.98	11.54	12.26	10.16	13.40	7.70	16.26
7	6.00	6.00	6.00	6.00	5.99	5.99	5.68	5.78	4.70	5.17	2.99	4.34
13	3.77	3.77	3.77	3.77	3.76	3.76	3.55	3.51	2.85	2.66	1.59	0.94

Table 4.2a Notes:

1. All errors listed in Table 4.2a are negative, i.e., $\left| \frac{\Phi_{\text{CALC}}}{\Phi_{\text{EXACT}}} \right| < 1$
2. α is in units of degrees. Refer to Fig. 4.4.
3. 'S' denotes unit-strength source distribution. 'D' denotes unit-strength dipole distribution.
4. Bezier surface degree = 3.

Table 4.2b Quadrature test errors (in percent) for *spherical* TRI panel, with $\alpha = 0.1$ degree and various θ .

Num PTS	$\theta = 0.1$		$\theta = 1$		$\theta = 5$		$\theta = 30$		$\theta = 60$		$\theta = 90$	
	S	D	S	D	S	D	S	D	S	D	S	D
1	25.00	25.00	25.00	25.00	23.78	30.23	25.29	25.48	26.23	26.94	28.03	29.46
3	10.00	10.00	10.00	10.00	8.36	11.29	10.12	9.89	10.50	9.57	11.24	9.12
4	11.98	11.98	11.98	11.98	10.20	13.39	12.12	11.94	12.57	11.85	13.41	11.75
7	6.00	6.00	6.00	6.00	4.73	5.09	6.07	5.73	6.28	4.98	6.68	3.93
13	3.77	3.77	3.77	3.77	2.86	2.54	3.81	3.42	3.94	2.42	4.16	1.02

Table 4.2b Notes:

1. All errors listed in Table 4.2b are negative, i.e., $\left| \frac{\Phi_{\text{CALC}}}{\Phi_{\text{EXACT}}} \right| < 1$
2. θ is in units of degrees. Refer to Fig. 4.4.
3. 'S' denotes unit-strength source distribution. 'D' denotes unit-strength dipole distribution.
4. Bezier surface degree = 3.

Table 4.2c Quadrature test errors (in percent) for *spherical* TRI panel, with $\theta = \alpha$.

Num PTS	$\theta = 1$ $\alpha = 1$		$\theta = 5$ $\alpha = 5$		$\theta = 15$ $\alpha = 15$		$\theta = 30$ $\alpha = 30$		$\theta = 60$ $\alpha = 60$		$\theta = 90$ $\alpha = 90$	
	S	D	S	D	S	D	S	D	S	D	S	D
1	25.00	25.00	25.00	25.05	24.98	25.45	24.98	26.80	25.75	32.11	29.15	40.71
3	10.00	10.00	9.99	10.00	9.93	10.03	9.72	10.15	8.97	10.89	8.16	13.05
4	11.98	11.98	11.97	11.99	11.90	12.04	11.68	12.29	10.80	13.35	9.63	16.42
7	6.00	6.00	5.99	5.99	5.94	5.88	5.76	5.50	5.06	3.90	4.07	0.81
13	3.77	3.77	3.77	3.75	3.73	3.62	3.59	3.14	3.10	0.97	2.50	3.87

Table 4.2c Notes:

1. All errors listed in Table 4.2c are negative, i.e., $\left| \frac{\Phi_{\text{CALC}}}{\Phi_{\text{EXACT}}} \right| < 1$, **EXCEPT** for the entry in the last row and column (in bold).
2. θ and α are in units of degrees. Refer to Fig. 4.4.
3. ‘S’ denotes unit-strength source distribution. ‘D’ denotes unit-strength dipole distribution.
4. Bezier surface degree = 3.

4.7 Velocity Coupling

On any given panel, the computed velocity will be continuous and smooth, consistent with the properties of Bezier surfaces and functions (see Chapter 3). At panel interfaces, however, the velocity will not be continuous across the interface, in general.²⁵ A technique referred to as *velocity coupling* is used in an effort to improve the quality of the global velocity distribution. In addition, velocity coupling may yield an improvement in the accuracy of the solution for the potential.

Velocity coupling can be applied at any global node \mathbf{x} meeting the following criteria, subject to possible restrictions relating to ‘excessive stiffness’ in the matrix equation:

25. On an edge common to two panels, the velocity is continuous *along* the entire edge, provided the Bezier threads (geometrical and functional) are common to both panels.

- The node \mathbf{x} must be either an EDGE or VERTEX type node situated on an interface at which two or more panels are joined.
- The adjoining panels must be approximately tangent at the interface;

The first requirement is obvious. The second is based on intuition, and is reflected in the derivation of velocity coupling equations. Ideally, C^1 continuity exists at the interface, however this does not appear to be a strict requirement.

As an example, assume that QUAD panels with Bezier function of degree 3 are utilized for the potential distribution. Each QUAD panel will have 16 potential control points uniformly distributed over the panel, with 4 control points allocated to each edge. On any given edge common to two neighboring panels, C^0 continuity of the potential is ensured, as all four edge control points are common to both adjoining panels. However, at a given EDGE node, the velocity computed with respect to one panel (say, Panel A) will in general differ from the velocity computed with respect to the adjoining panel (Panel B). This comes as no surprise, since the neighboring panels are separate entities (with only C^0 continuity, geometrically and functionally) and collocation nodes (field points) are relatively sparse.²⁶ *Velocity coupling is essentially a process of equating two such computed velocities.*

Velocity coupling as described is essentially a collocation process, in the sense that the velocity is guaranteed to be continuous only at control points for which velocity-coupling is applied, and strictly speaking, is continuous nowhere else along the panel edge.

Velocity coupling produces an independent equation that can be ‘inserted’ into the matrix equation. If it is desired to avoid an overdetermined matrix system (which is the case in this thesis), the boundary integral equation associated with the field point \mathbf{x} may be supplanted by the velocity-coupling equation in the appropriate row of the influence matrix, with an appropriate change to the corresponding load vector element. Further aspects are discussed in Section 4.8.

26. True C^1 continuity can in principle be obtained among a collection of patches, in which case the individual patches become transformed into one large patch. This modified approach may offer some advantages, but is not pursued in this paper.

4.7.1 Velocity Coupling Equation

The general form of the velocity coupling equation is expressed as

$$\mathbf{d} \cdot \mathbf{V}^A(\mathbf{x}) = \mathbf{d} \cdot \mathbf{V}^B(\mathbf{x}), \quad (4.27)$$

where \mathbf{x} is a node on the interface between Panel A and Panel B, \mathbf{d} is a vector tangent to the body at \mathbf{x} , and \mathbf{V}^A and \mathbf{V}^B are velocity expressions given in terms of potential control points on Panel A and Panel B, respectively.

The velocity computation itself is discussed in Section 4.10. Fortunately, the velocity computation for nodes at a panel interface (edge or vertex) is simplified, compared to the general case. For example, consider a QUAD panel with degree 3 for the surface and degree 2 for the potential function. The first derivative evaluated at some point on the edge, with respect to a parameter line crossing the edge, depends on the row of control points lying on that edge, as well as the row of control points adjacent to the edge (i.e., a pair of Bezier threads on the edge and parallel to the edge, respectively). The derivative of the surface itself can be computed beforehand, and therefore the geometrical control points themselves do not enter into the velocity equation. For the derivative of the potential, the potential control point values (Bezier ordinates) are unknown and therefore must be incorporated into the velocity equation explicitly. As the degree is 2, there will be 3 x 3 rows of potential control points; the first derivative with respect to a parameter crossing the edge on which the node is located will involve a total of six control points; more specifically, there will be three pairs of differences taken between the two Bezier threads.

Refer to Chapter 3 for derivative expressions.

4.8 Assembly of Linear System of Equations

The exact form of the discretization depends on several factors, including the type of matrix system envisaged. The implementation programmed in this thesis is a matrix equation of the following type:

$$\mathbf{A} \cdot \boldsymbol{\varphi} = \mathbf{c} \quad (4.28)$$

where \mathbf{A} is a square influence matrix, $\boldsymbol{\varphi}$ is the vector of unknown potential ordinates, and \mathbf{c} is a known right-hand side vector. Other aspects of this equation were discussed in Section 4.4.

An alternate approach could utilize an equality-constrained least-squares (LSE) matrix system, with suitable constraint equations, e.g., see [Lee 99], and also [Golub 96] for further details on this matrix method. In this thesis, however, the LSE approach was not pursued.

As with any panel method, assembly of the influence matrix \mathbf{A} is the primary task at hand. In the method implemented here, the influence matrix is constructed one row at a time. Each row is associated with two key variables: a prescribed field point for which the left-hand side of the integral equation (4.9) or (4.20) is applied, and a corresponding potential control point (Bezier ordinate) of unknown value. The latter constitutes an element in the vector of unknowns, $\boldsymbol{\varphi}$, discussed in more detail in Section 4.4.

4.8.1 Boundary Integral Equation

The boundary integral equation is the foundation of the method and therefore plays the most important role in characterizing the matrix equation. In principle, a square matrix equation can be generated solely from the discrete form of the boundary integral equation, by assembling M instances of the equation corresponding to M unique field points (the lifting-body problem requires an auxiliary equation (Kutta condition) as discussed in Chapter 2 and Section 4.8.3).

4.8.2 Velocity-coupling Equation

Independent equations of the velocity-coupling type presented in Section 4.7 can be used in lieu of the boundary integral equation (only for field points located at panel interfaces). One significant advantage of the velocity-coupling equation is the fact that the number of operations required to assemble the row in the influence matrix is far less than required by the boundary integral equation.

4.8.3 Kutta Condition

A third type of independent equation is required for the lifting-body problem, as discussed in Chapter 2. The most general statement of the Kutta condition, (2.7), leads to a variety of methods to implement the Kutta condition for computational purposes, depending on the application and analysis method, e.g., see [Kerwin 78]. As discussed in [Kerwin 87] and [Lee 99], the Kutta condition can be characteristically kinematic or dynamic, or a combination of both.

In principle, the Kutta condition may be imposed at the trailing edge, at each location where a pair of opposing control points exists. See Figure 4.9. Using a technique similar to that employed for velocity coupling (described in Section 4.7), it is possible to write an equation in terms of the potential control points (Bezier ordinates) located on both ‘sides’ of the foil.

As indicated in Fig. 4.9b, the question arises as to whether a double-node should exist on the trailing edge at the ends of the span, where the trailing edge curve C_{TE} is reentrant. Since a dipole sheet (with dipoles oriented normal to sheet) is equivalent to a distribution of vorticity (tangential to the sheet) of strength equal to the local rate of change of the dipole strength, plus a vortex filament at the edge of the sheet with strength equal to the strength of the dipole, one may conclude that the use of a single node at the ‘edge’ of the wake sheet would result in an equivalence of a zero-strength vortex filament at the edge of the wake.²⁷ If the equivalence of a finite-strength vortex filament is desired at the edge of the wake sheet, then there must be two independent control points to allow a difference in potential to exist, just as with the remaining intermediate trailing edge control point ‘pairs’.

27. Recall that the wake sheet really comprises a pair of dipole sheets, with opposite normal vectors, cf. Fig. 2.1. Use of one independent node (control point) at the end of the span is, in electrical engineering parlance, akin to ‘shorting’ the two dipole sheets, thus resulting in zero difference of potential along the edge of the wake progressing downstream.

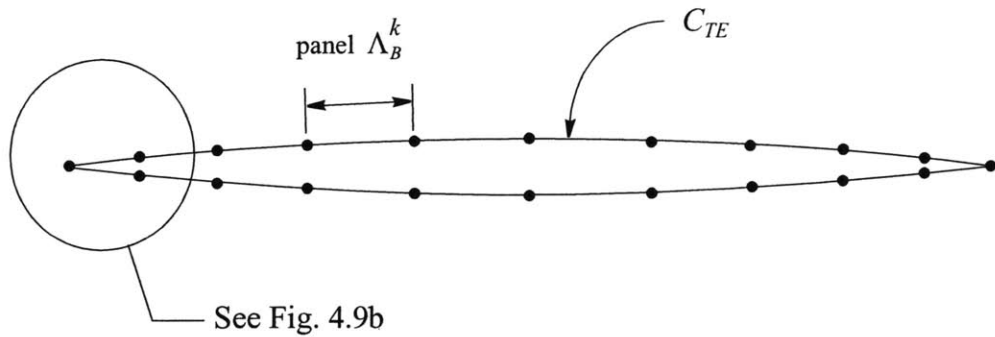

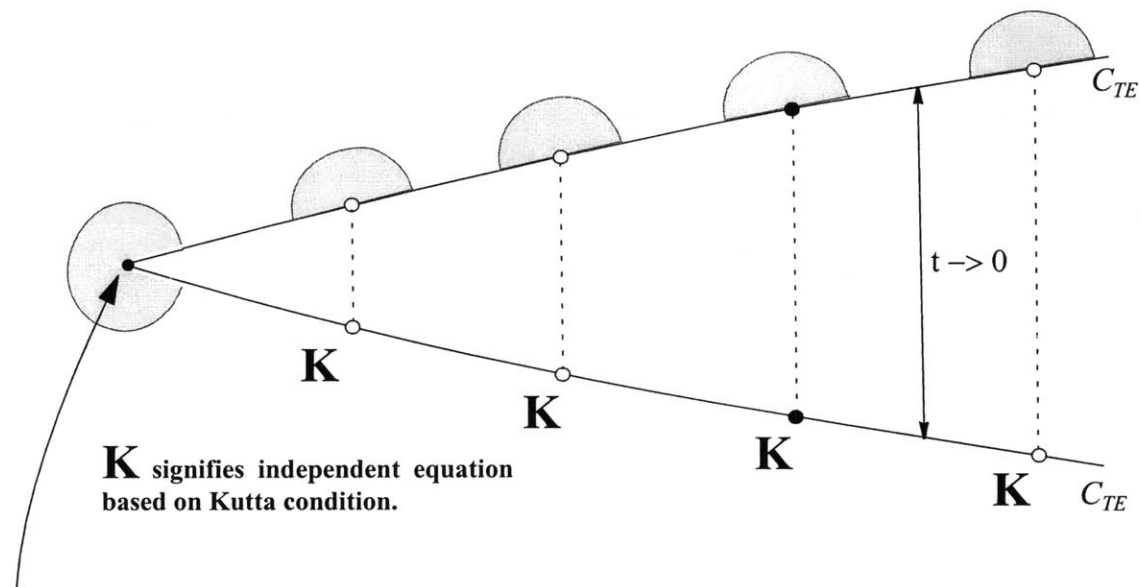


Fig. 4.9a Schematic of trailing edge discretization. The trailing edge is a closed curve as denoted by C_{TE} .

 Symbolizes use of Green's theorem (boundary integral equation) at node (field point).



K signifies independent equation based on Kutta condition.

Reentrant node on TE:
 A question arises as to whether this should be a 'double node'. A double node allows a potential difference at the edge of the wake sheet, thus permitting the equivalence of a non-zero vortex filament strength at this location.

- vertex node
- edge node

Fig. 4.9b

Close-up of panel nodes at the trailing edge, near the end of the wing span. Opposing trailing edge nodes are joined by dotted lines. For a zero-thickness trailing edge ($t_{TE} = 0$), opposing nodes occupy the same location; in this figure they are shown separated to clarify the different treatment of the nodes.

4.9 Solution of Matrix Equation

In the first-generation implementation of this higher-order panel method, the solution of the matrix equation was carried using LU decomposition and back-substitution [Press 92]. This method was utilized for expediency. No attempt was made to incorporate alternative matrix solution techniques, however other researchers have obtained substantial improvements in computational performance (relative to Gauss reduction) by employing accelerated iterative solution procedures. See, for example [Lee 87].

4.10 Velocity Computation

Velocity computations are performed after a solution of the matrix equation is obtained. The process involves the computation of two derivatives with respect to the parameter u or v . One derivative, $d\phi/dt$ relates the velocity potential to the Bezier parameter, while the other, ds/dt , relates the physical coordinate to Bezier parameter. Here dt represents either du or dv , and ds is the differential arc length (actual physical coordinate). These derivatives are combined in accordance with the chain rule. A similar procedure as applied to a B-spline panel method is outlined in [Lee 99].

Derivative formulae for the Bezier surface and scalar function are provided in Chapter 3. Only the first derivatives enter into the calculation of the velocity.

Chapter 5

Test Cases

5.1 Steady Flow Past Sphere

The steady incompressible potential flow over a sphere was analyzed using a first-generation implementation of the Bezier-based higher order panel method. The test sphere for which results are presented is shown in Fig. 5.1.

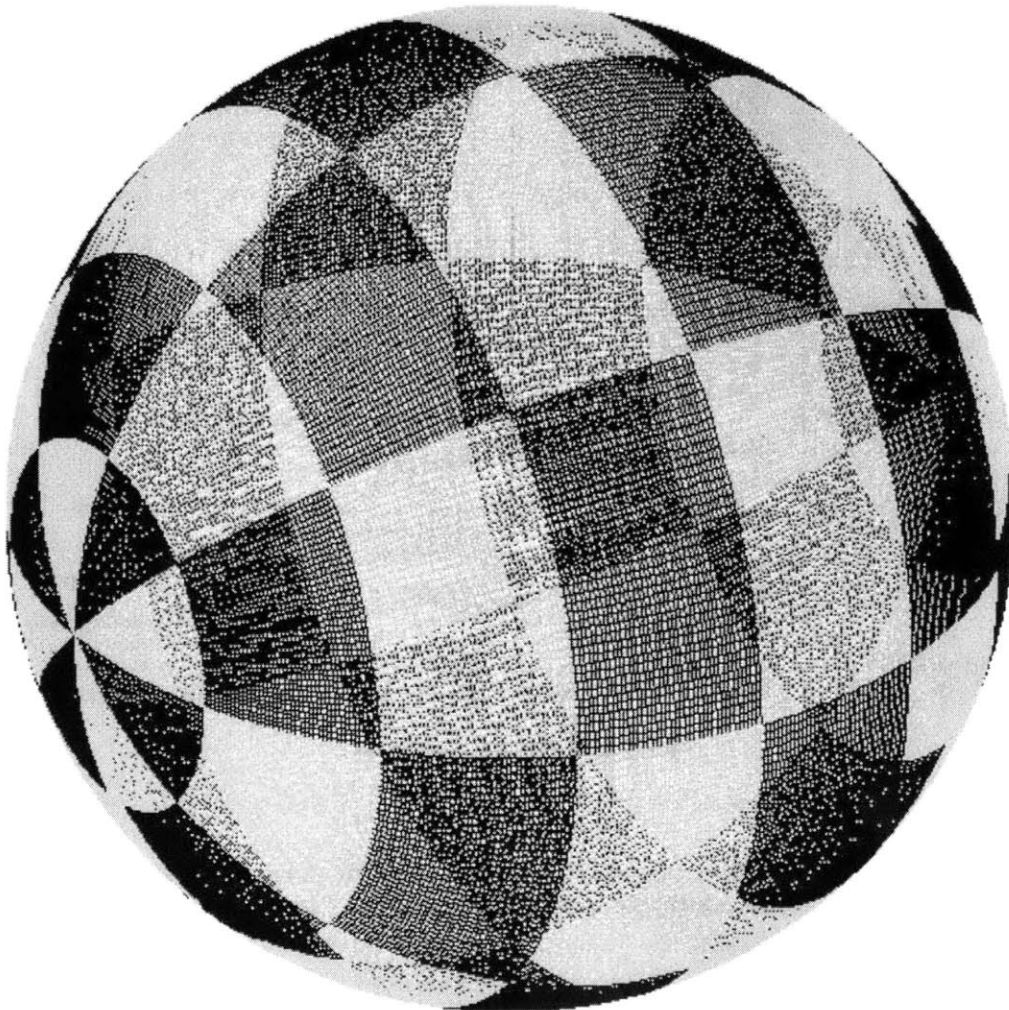


Fig. 5.1 Discretization of spherical body, 8 x 8 panels (meridional x circumferential).

Fig. 5.2 compares the computed total potential and velocity with exact values. Overall agreement is seen to be very good. As might be expected, there is closer agreement between the potential, versus the velocity. The maximum error in velocity occurs near the poles of the sphere, where the TRI panels are located; this error may be partially attributed to the velocity algorithm for TRI panels, which needs further validation.

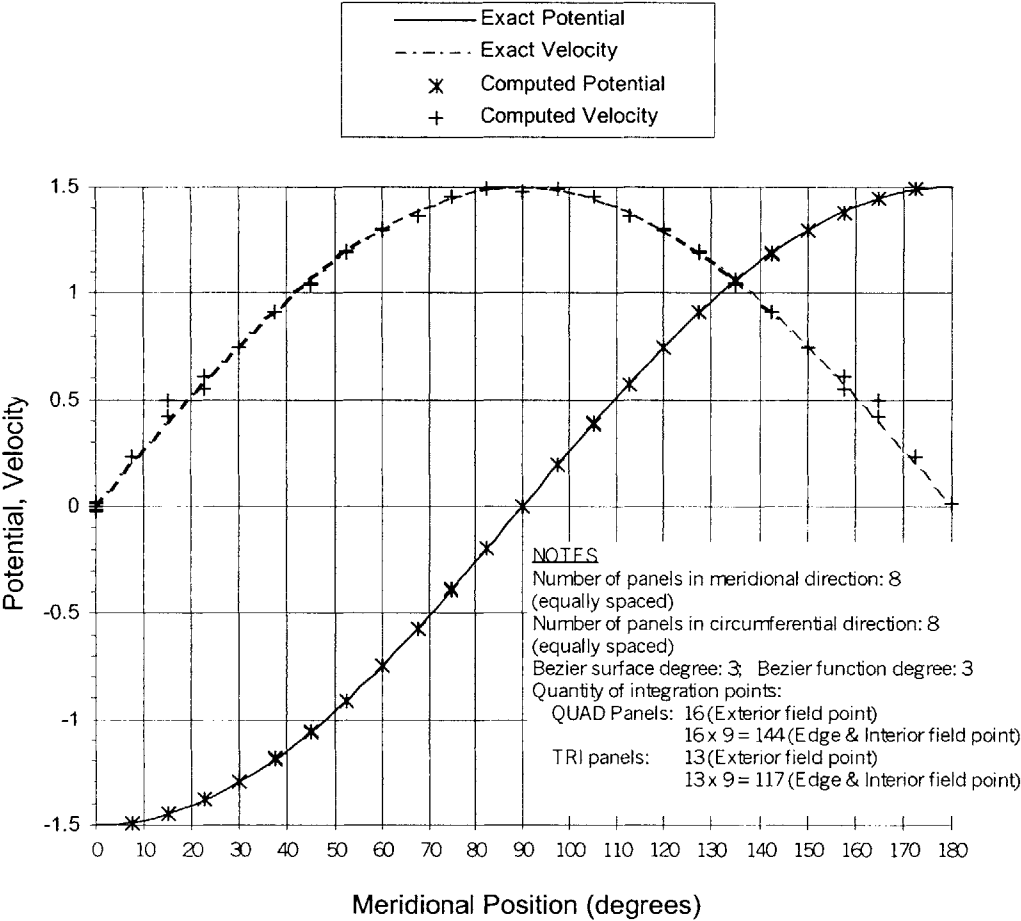


Fig. 5.2 Comparison of computed and exact potential (total) and meridional velocity for spherical body shown in Fig. 5.1.

5.2 Added Mass of Spheroids

An added-mass computational routine was developed using the perturbation-potential formulation discussed in Chapters 2 and 4. The added-mass computation is based on well-known relations, given, e.g., in [Newman 77].

Test cases were run on spheroidal bodies (i.e., ellipsoids of revolution) with beam-length ratio varying from 0.1 to 1.5. A typical spheroid is shown in Fig. 5.3, which also illustrates a typical panel arrangement. Three components of added-mass were computed:

- m_{11} - surge component
- m_{22} - sway component
- m_{55} - yaw component

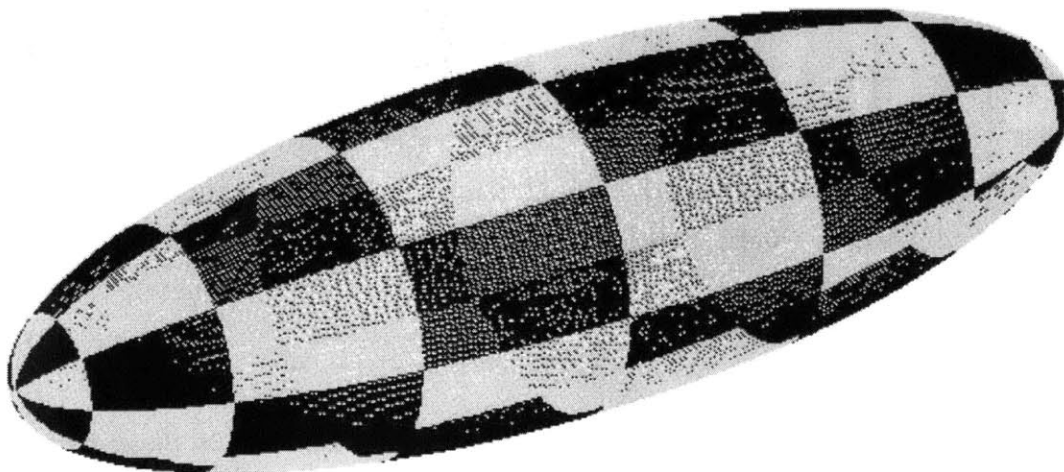


Fig. 5.3 Discretization of spheroid. Beam-length ratio = 0.3.
Panel Discretization: 8 x 8.

Comparisons of computed and exact values are shown in Fig.'s 5.4, 5.5 and 5.6, for m_{11} , m_{22} , and m_{55} , respectively. The agreement is very good for all three components.

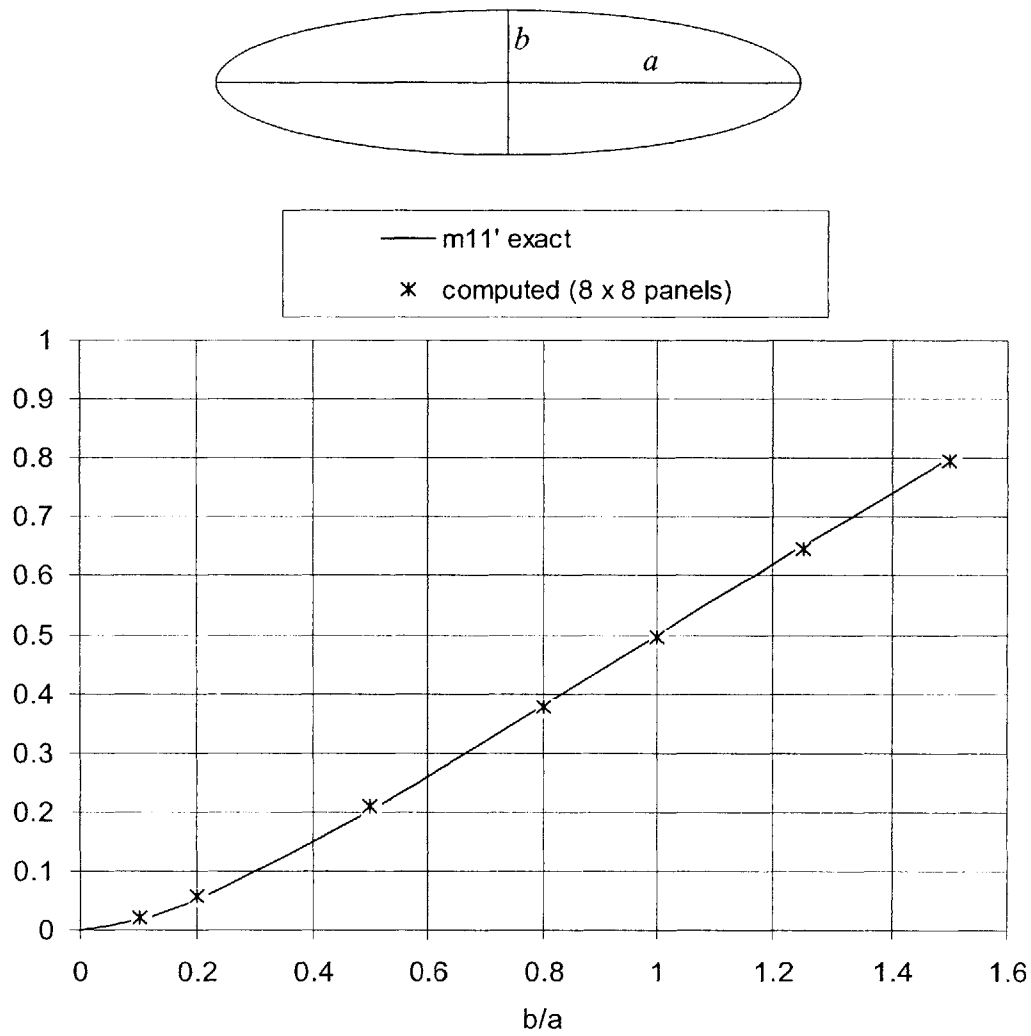


Fig. 5.4

Added-mass coefficient m_{11} for a spheroid of length $2a$ and midbody diameter of $2b$. Bezier degree 3 for both surface and potential function. The added mass m_{11} denotes surge acceleration (longitudinal direction). The coefficient is nondimensionalized with respect to the mass of the displaced volume of fluid, which is $(4/3)\pi\rho ab^2$. See [Newman 77] for further details.

NOTE: The 'exact' curve shown was manually extracted from Fig 4.8 in [Newman 77], i.e., it is not an exact reproduction of that curve. Accordingly, there may be a small error in translation.

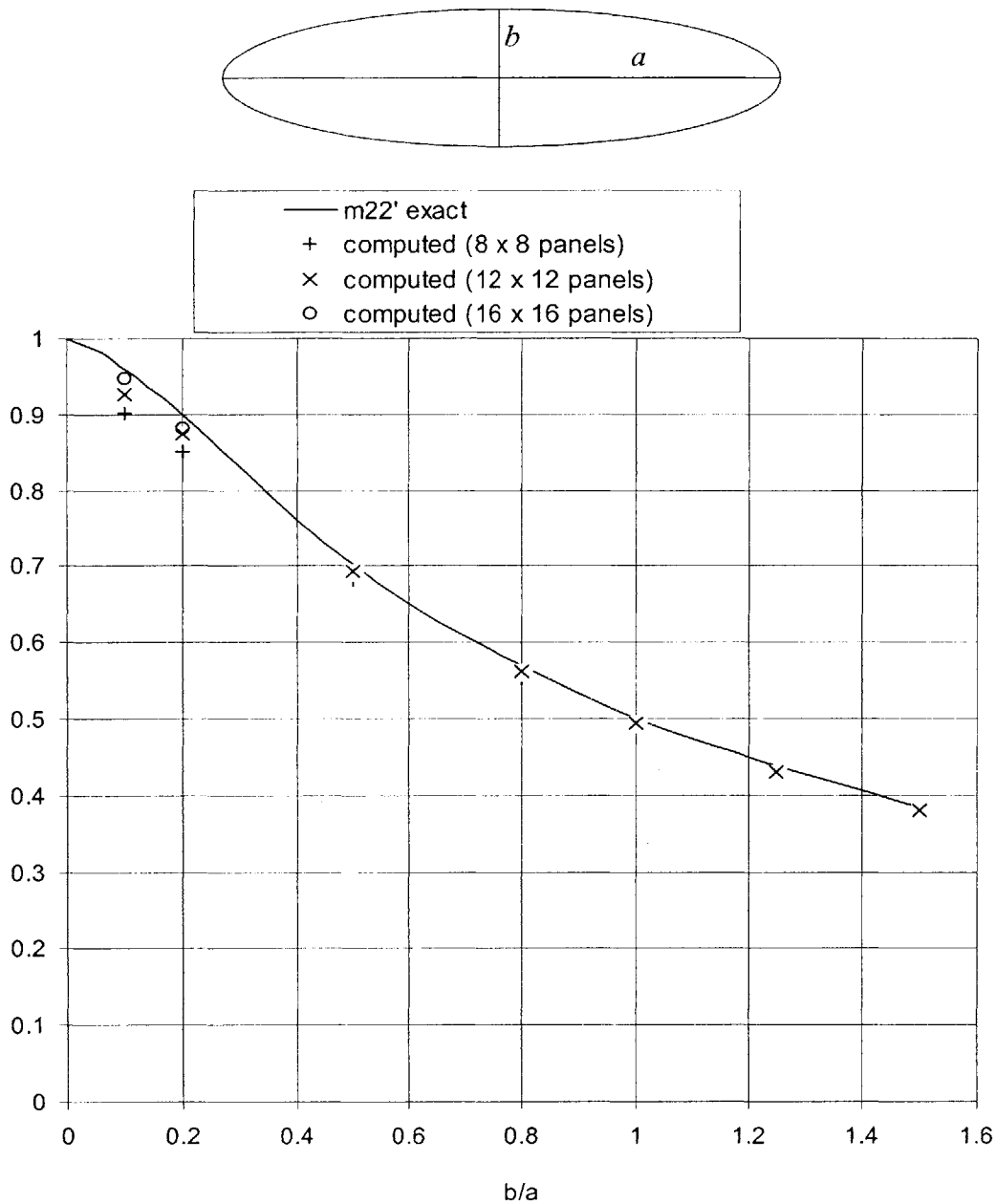


Fig. 5.5

Added-mass coefficient m_{22} for a spheroid of length $2a$ and midbody diameter of $2b$. Bezier degree 3 for both surface and potential function. The added mass m_{22} denotes sway acceleration (lateral, in equatorial plane). The coefficient is nondimensionalized with respect to the mass of the displaced volume of fluid, which is $(4/3)\pi\rho ab^2$. See [Newman 77] for further details.

NOTE: The 'exact' curve shown was manually extracted from Fig 4.8 in [Newman 77], i.e., it is not an exact reproduction of that curve. Accordingly, there may be a small error in translation.

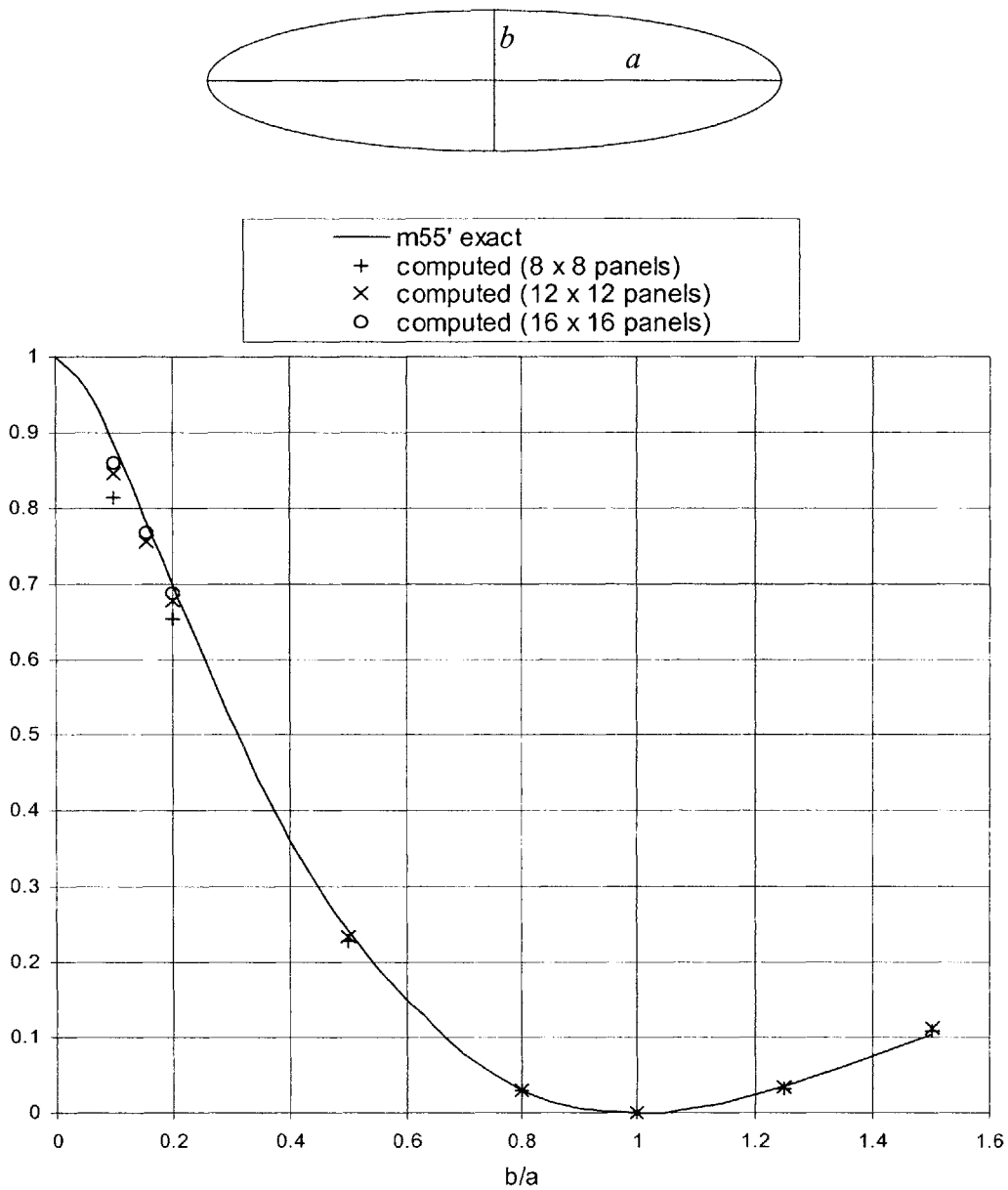


Fig. 5.6

Added-mass coefficient m_{55} for a spheroid of length $2a$ and midbody diameter of $2b$. Bezier degree 3 for both surface and potential function. m_{55} denotes the added moment of inertia for rotation about an axis in the equatorial plane. The coefficients are nondimensionalized with respect to the moment of inertia of the displaced volume of fluid, which is $(4/15)\pi\rho ab^2(a^2 + b^2)$. See [Newman 77] for further details.

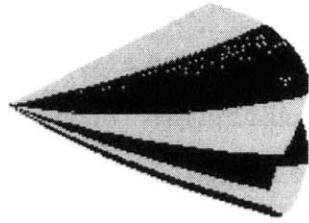
NOTE: The 'exact' curve shown was manually extracted from Fig 4.8 in [Newman 77], i.e., it is not an exact reproduction of that curve. Accordingly, there may be a small error in translation.

5.3 Sample Discretization of Hydrofoil

In order to illustrate the use of a TRI panel arrangement at the tip of a wing or hydrofoil, a sample discretization was generated, as shown in Fig. 5.7. In this example, TRI panels are used exclusively at the tips. The arrangement shown differs from a typical treatment of the tip region, in which a small portion of the tip remains ‘undiscretized’, due to the exclusive use of quad-like panels, for which it is not practical to ‘close the gap.’

The close up view of the tip region shows quite thin sliver-like panels in way of the leading edge. From a numerical viewpoint this is not necessarily cause for alarm; as discussed in Section 4.5, the single-panel quadrature tests performed for a spherical TRI patch showed that the error did not significantly increase with increasing aspect ratio (ratio of θ to α , cf. Fig. 4.4 and Table 4.2b). One parameter that has a bigger impact on accuracy is the amount of ‘curl’ exhibited by the panel, i.e., the total change in α and θ (roughly speaking, the amount of variation in the normal vector while traversing from one end of the panel to another).

Whether or not the type of arrangement shown in Fig. 5.7 presents any advantage remains to be seen.



CLOSE-UP OF TIP REGION

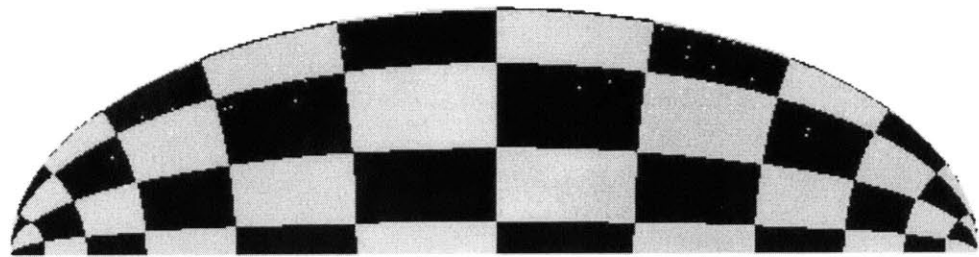
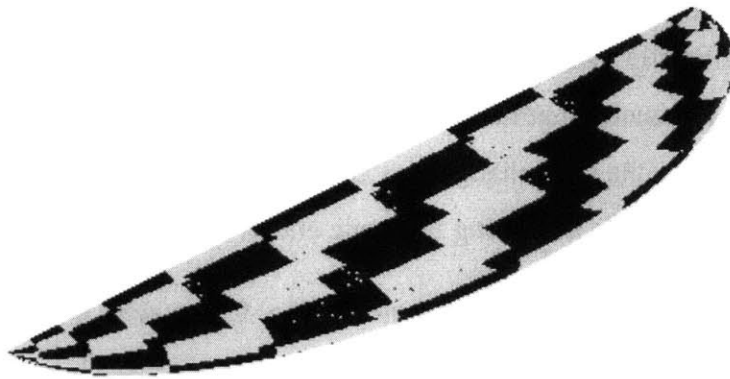


Fig. 5.7

Sample discretization of a symmetrical-section hydrofoil with elliptical planform, showing use of TRI panels at both ends of the span.

Chapter 6

Conclusions

The Bezier-based higher order panel method developed in this thesis performs well with respect to the test cases presented in Chapter 5: *a)* steady flow past a sphere, and *b)* added mass of spheroids. In both cases, very good agreement with exact values was demonstrated. For these cases, at least, it appears that standard Gauss-Legendre quadrature provides an adequate means of facilitating the task of computing the boundary integrals. In the method outlined herein, a field point is never permitted to lie in the interior of the quadrature domain; for field points that lie inside the perimeter of a panel, a subdivision is utilized. Of course, the efficacy of this strategy depends on how well the quadrature method can handle singularities on the boundary of the quadrature subdomain.

The single-panel quadrature tests summarized in Chapter 4 confirm that the accuracy of Gauss-Legendre quadrature generally does not match that of some other methods described in the literature (for equal number of integration points), nonetheless, the foregoing results attest to its effectiveness in those cases. In any case, the Bezier-based panel method does not preclude the use of other methods of quadrature.

In general, the quality of the geometrical parameters appears to play an important role in the overall performance of the method. The incorporation of Bezier panels is likely a significant contributory factor in the favorable results witnessed so far, as Bezier patches provide an extremely stable and consistent platform for determination of coordinates, derivatives and Jacobians over the panel. Moreover, as the quadrature domain never extends beyond the perimeter of a panel, the issue of higher-order continuity between panel interfaces does not appear to be critical.

A preliminary formulation for the lifting-body case has been presented, however, further development and testing is required in order to ascertain the validity of the method for this problem class. From a geometric standpoint, the Bezier representation appears to present some advantages over some other methods, as both triangular and tensor-product (four-sided) patches can be utilized, giving the analyst more flexibility in choosing panel arrangements. Again, this is consistent with the view that high fidelity in geometric modeling is desirable, especially in certain applications.

The velocity coupling technique presented appears to perform as intended, although more testing is required in general to ascertain whether the benefit is consistently achieved, particularly for interfaces between triangular panels. Besides yielding a smoother velocity distribution, there are indications that the overall solution of the potential is improved when velocity coupling is judiciously applied. Worth noting is the contrast in equation assembly time between the two equation types (i.e., velocity-coupling vs. Green's theorem). The 'rapid-fire' execution time of the velocity-coupling equation comes as a welcome bonus.

Results of this initial investigation indicate that further development work on the Bezier-based panel method may be warranted, depending on foreseeable needs. The method will require further effort to determine whether it is suitable for the lifting-foil problem. There is the possibility that the Bezier-based method may be of utility in other fields in which boundary element methods are commonly utilized (e.g., electromagnetics).

Bibliography

- [Aliabadi 89] Aliabadi, M.H.; Hall, W.S.: The regularising transformation integration method for boundary element kernels. Comparison with series expansion and weighted Gaussian integration methods. *Engineering Analysis with Boundary Elements*, Vol. 6, No.2, (1989) 66-71.
- [Arfken 85] Arfken, G.: *Mathematical Methods for Physicists*, 3rd ed., Academic Press, 1985.
- [Brebbia 89] Brebbia, C.A.; Dominguez, J.: *Boundary Elements, An Introductory Course*, Computational Mechanics Publications, co-published with McGraw-Hill, 1989.
- [Chari 00] Chari, M.V.K; Salon, S.J.: *Numerical Methods in Electromagnetism*, Academic Press, 2000.
- [Cowper 73] Cowper, G.R.: Gaussian Quadrature Formulas for Triangles. Short communication, *Int. J. Num. Meth. Engng*, Vol 7, Issue 3 (1973) 405-408.
- [Farin 99] Farin, G.: Computer-Aided Geometric Design. in Thomson, J.F; Soni, B.K.; Weatherill, N.P. (ed): *Handbook of Grid Generation*, Chapter 28, CRC Press, 1999.
- [Freund 80] Freund, J.E.; Walpole, R.E.: *Mathematical Statistics*, 3rd ed., Prentice-Hall, 1980.
- [Funaro 92] Funaro, D.: *Polynomial Approximation of Differential Equations*, Springer-Verlag, 1992.
- [Golub 96] Golub, H.G.; Van Loan, C.F.: *Matrix Computations*, 3rd ed., John Hopkins University Press, 1996.
- [Hess 64] Hess, J.L.; Smith, A.M.O.: Calculation of Nonlifting Potential Flow About Arbitrary Three-Dimensional Bodies. *Journal of Ship Research*, Vol. 8, No. 2, Sept. 1964.
- [Hess 67] Hess, J.L.; Smith, A.M.O.: Calculation of Potential Flow About Arbitrary Bodies. *Prog. Aeronaut. Sci.* 8 (1967) 1-138.

- [Hess 72] Hess, J.L.: Calculation of Potential Flow About Arbitrary Three-Dimensional Lifting Bodies. McDonnell Douglas Corp. Report No. MDC J5679-01, October 1972.
- [Hess 87] Hess, J.L.; Valarezo, W.O.: Application of an Advanced Panel Method to Aerodynamic Problems of Aircraft Design, in *Panel Methods in Fluid Mechanics with Emphasis on Aerodynamics, Proc. of the Third GAMM-Seminar, Kiel*, January 1987.
- [Hoschek 93] Hoschek, J.; Lasser, D.: *Fundamentals of Computer Aided Geometric Design*, A.K.Peters, 1993.
- [Hsin 90] Hsin, C.-Y.: Development and Analysis of Panel Methods for Propellers in Unsteady Flow. Ph.D. thesis, M.I.T., Department of Ocean Engineering, 1990.
- [Hsin 91] Hsin, C.-Y.; Kerwin, J.E.; Kinnas, S.A.: A Panel Method for the Analysis of the Flow Around Highly Skewed Propellers, *Proc. SNAME Propellers/Shafting '91 Symp., Virginia Beach, VA*, Paper No. 11.
- [Hunt 80] Hunt, B.: The Mathematical Basis and Numerical Principles of the Boundary Integral Method for Incompressible Potential Flow over 3-D Aerodynamic Configurations, in *Numerical Methods in Applied Fluid Dynamics*, Academic Press (1980) 49-135.
- [Jerri 99] Jerri, A.J.: *Introduction to Integral Equations with Applications*. 2nd ed, Wiley-Interscience, 1999.
- [Kerwin 78] Kerwin, J.E.; Lee, C.-S.: Prediction of Steady and Unsteady Marine Propeller Performance by Numerical Lifting-Surface Theory, *SNAME Transactions*, Vol. 86, (1978) 218-253.
- [Kerwin 87] Kerwin, J.E.; Kinnas, S.A.; Lee, J.-T.; Shih, W.-Z.: A Surface Panel Method for the Hydrodynamic Analysis of Ducted Propellers, *SNAME Transactions* 1987.
- [Lamb 32] Lamb, H.: *Hydrodynamics*, 6th ed., Cambridge University Press, 1932, reprint by Dover, 1945.

- [Lean 85] Lean, M.H.; Wexler, A.: Accurate Numerical Integration of Singular Boundary Element Kernels Over Boundaries with Curvature. *International Journal for Numerical Methods in Engineering*, Vol. 21, (1985) 211-228.
- [Lee 99] Lee, C.-S.; Kerwin, J.E.: A B-Spline Higher Order Panel Method for Analysis of Steady Flow around Marine Propellers, 1999 (preliminary draft).
- [Lee 87] Lee, J.-T.: A Potential Based Panel Method for the Analysis of Marine Propellers in Steady Flow, Ph.D. thesis, M.I.T., Department of Ocean Engineering, 1987.
- [Lighthill 86] Lighthill, J.: *An Informal Introduction to Theoretical Fluid Mechanics*. Oxford University Press, 1986.
- [Mohr 92] Mohr, G.A.: *Finite Elements for Solids, Fluids, and Optimization*. Oxford University Press, 1992.
- [Moran 84] Moran, J.: *An Introduction to Theoretical and Computational Aerodynamics*, Wiley, 1984.
- [Morino 74] Morino, L.; Kuo, C.-C.: Subsonic Potential Aerodynamics for Complex Configurations: A General Theory, *AIAA Journal*, Vol. 12, No. 2 (1974) 191-197.
- [Newman 77] Newman, J.N.: *Marine Hydrodynamics*, MIT Press, 1977.
- [Patera 95] Patera, A.T.: 2.274 Computational (Incompressible) Fluid Dynamics Lecture Notes on Basic Material. M.I.T., Department of Mechanical Engineering, 1995.
- [Press 92] Press, W.H.; Teukolsky, S.A.; Vetterling, W.T.; Flannery, B.P.: *Numerical Recipes in C*, 2nd ed., Cambridge University Press, 1992.
- [Pyo 94] Pyo, S.; Kinnas, S.A.: The Flow Adapted Grid (FLAG) Applied to the Analysis of Propeller Tip Flows, *Proc. SNAME Propellers/Shafting '94 Symp., Virginia Beach, VA*, Paper No. 10.
- [Robertson 65] Robertson, J.M.: *Hydrodynamics in Theory and Application*, Prentice-Hall, 1965.

- [Sclavounos 87] Sclavounos, P.D.: A note on a Galerkin technique for integral equations in potential flows. *Journal of Engineering Mathematics* 21 (1987) 101-114.
- [Tricomi 57] Tricomi, F.G.: *Integral Equations*, Interscience, 1957, reprint by Dover, 1985.
- [Zienkiewicz 94] Zienkiewicz, O.C.; Taylor, R.L.: *The Finite Element Method*, 4th ed., Vol 1, McGraw-Hill, 1994.

2766-89